

with

$$v_{brine} = Sp(T) \frac{\rho}{\rho_{ice}} \quad (52)$$

used to calculate the ice volume yields negative values. Here is  $v_{ice}$  the volume of the fresh water ice,  $v_{brine}$  the volume of the brine and  $v_{air}$  the volume of the air bubbles in the sea ice.  $S$  is the salinity,  $p$  the temperature dependency (monotonical increasing function of temperature  $T$ ),  $\rho$  the density of the ice and  $\rho_{ice}$  the density of the pure water ice. In physical terms, this means that the ice would actually melt away because there is too much salt. Realistic values for the bulk salinity of most sea ice range from 0 to 15 ‰ except at the very surface where the salinity can be higher. The density of the number of bubbles should not be so great that the bubbles overlap. One grain of sea ice represents a packet of brine pockets sandwiched into the lamellar structure with fresh water ice. Crystallographic analysis shows that it is a single crystal. Typical grain sizes should be several mm. The parameter BRATIO describes the square of the ratio of the horizontal and the vertical dimension of the brine pockets. For warmer ice a typical value should be  $2.5 \times 10^{-5}$  increasing to 0.1 near the surface representing more spherical brine pockets. It affects primarily the volume scattering (which is small in first-year ice types, i.e. thin ice, young ice and firstyear ice). The zenith angle of the brine pocket affects primarily the cross polarized scattering coefficients. Typical values are between  $0^\circ$  and  $10^\circ$  and not greater than  $30^\circ$ .

**3.1.2.2 The snow layers** The basic constituents of snow are air, ice, and, for wet snow, water. The ice volume fraction  $v_{ice}$  is calculated from the density  $\rho$  and the volume fraction of the free water  $v_w$  (called pendular water) with the following formula:

$$v_{ice} = \frac{(\rho - v_w)}{0.917}. \quad (53)$$

Here 0.917 is the density of fresh water ice. The dielectric constant of air is set to 1. The dielectric constant uses the results of Maetzler and Wegmueller (1987). They did measurements from 2 to 100 GHz by a resonator method (2–10 GHz) and a radiometer method (10–100 GHz) with pure and slightly saline (10 to 13 ‰) ice. The model assumes a film of water around every ice grain (Strogryn 1986). The volume fraction  $v_f$  of the water in the film is calculated with the empirical formula

$$v_f = f_w v_w = (0.261 - 0.724 v_w) v_w. \quad (54)$$

Here  $v_w$  is the total volume fraction of free water in the snow and  $f_w$  is the fraction of water in the film around the ice grains.  $f_w$  was estimated on the basis of the dielectric data of Linlor (1980). The dielectric constant of the free water is calculated with an empirical formula of Strogryn (1971). The model assumes that the pendular water is free of salt. As a consequence, the dielectric constant of the pendular water is the one of fresh

water. The correlation function to calculate the scattering contribution for the effective dielectric constant tensor is spherically symmetric implying isotropic radiation properties of the snow.

Typical values for the density of the snow are between 0.05 and 0.5 g/cm<sup>3</sup>. The snow grain diameter can be up to 1 cm. Typical values are between 0.05 and 2 mm. The temperature of the snow is below 273 K, otherwise it will transform into a puddle of water.

**3.1.2.3 The Water-Layer** The strong-fluctuation-theory decomposes the effective dielectric tensor into a quasi-static dielectric tensor and a scattering contribution dielectric tensor. In the case of a water layer the quasi-static tensor has only identical diagonal elements. The components of the effective dielectric tensor are identical to the components of the quasi-static dielectric tensor.

The dielectric constant is represented according to Stogryn (1971) by an equation of the Debye form

$$K = \epsilon_{\infty} + \frac{\epsilon_S - \epsilon_{\infty}}{1 - i2\pi\tau\nu} + i \frac{\sigma}{2\pi\epsilon_0\nu} \quad (55)$$

where  $\epsilon_S$  and  $\epsilon_{\infty}$  are, respectively, the static and high-frequency dielectric constants of the solvent (modified by the solute),  $\tau$  is the relaxation time,  $\epsilon_0$  is the permittivity of free space,  $\sigma$  is the ionic conductivity of the dissolved salts,  $i = \sqrt{-1}$ , and  $\nu$  is the electromagnetic frequency. For greater details see Stogryn (1971).

### 3.1.3 Some results of the ice-module

In this section we present some typical results which we obtained from the ice-module alone.

The program calculates the horizontal and vertical emissivities and brightness temperatures based on an input file containing the physical parameters for the different layers (Table 3). The physical parameters are the layer thickness, the temperature, density, diameter of the snow grains, free water content of the snow, the diameter of the ice grains, the diameter of the air bubbles, the salinity, the brine angle and the ratio of the brine pocket diameters. The parameters which we have analysed are the horizontal and vertical polarized emissivities in the microwave range between 1 and 100 GHz. First we show results for multiyear ice with and without snow. The radiometric data are from the CEAREX-experiment in the Barents Sea (Arctic) at Drift-Station 7, described in Winebrenner et al. (1992). To model the ice structure we have used the parameter-set of Table 3. One of the important parameters is the snow grain size. For more details see the sensitivity analysis. In the horizontally polarized radiometric data we have two different minima. If we change

Table 3 Parameters of multiyear ice from the Barents Sea used for the model calculations (see Table 2 for symbols).

type	$z$	$T$	$\rho$	$D_{GS}$	$l_f$	$D_{GI}$	$D_B$	$S$	$\theta_B$	$B_R$
	[m]	[K]	[g/cm <sup>3</sup> ]	[mm]	[-]	[mm]	[mm]	[%o]	[°]	[-]
snow	0.20	263.1	0.100	0.8	0.0	0.0	1.2	0.0		1.0
	0.10	263.1	0.100	0.8	0.0	0.0	1.2	0.0		1.0
	0.05	263.3	0.460	0.8	0.0	0.0	5.0	0.0		1.0
	0.00	263.5	0.728	0.8	0.0	0.0	3.0	0.0		1.0
ice	-0.18	263.7	0.895		0.0	10.0	1.2	0.1	24.0	0.25E-4
	-0.26	264.1	0.895		0.0	10.0	1.2	0.3	24.0	0.25E-4
	-0.43	264.5	0.895		0.0	10.0	1.2	0.7	24.0	0.25E-4
	-0.57	264.8	0.895		0.0	10.0	1.2	1.2	24.0	0.25E-4
	-0.67	265.1	0.890		0.0	10.0	1.2	1.4	24.0	0.25E-4
	-0.77	265.4	0.890		0.0	10.0	1.2	1.9	24.0	0.25E-4
	-0.82	265.4	0.890		0.0	10.0	1.2	2.4	24.0	0.25E-4
	-1.38	266.1	0.870		0.0	10.0	1.2	3.0	24.0	0.25E-4
water		269.9	1.000		1.0			32.0		

the snow grain size to lower values we get the minimum of the theoretical data at higher frequencies. This follows e.g. from a comparison with the modeling in Winebrenner et al. (1992).

One typical result from measurements of multiyear ice is that the density of the uppermost ice layer is lowered according to brine drainage. Figure 32 shows the influence of this effect to the microwave signal.

For frequencies in the range of 10 to 40 GHz we get lower emissivities in the case of lower density. The influence is not very great but is strongly influenced by the snow layer. If we put away the snow layer we find a greater influence of the change of density on the horizontal polarized radiometric signal because the ice layer is now the uppermost layer. Since we have now two layers of ice with different dielectric constants according to the different densities we get an interference effect at the boundary layer between the two ice layers. The influence on the vertically polarized emissivity is low. For the horizontally polarized signal we have found the opposite effect like in the case of ice with snow layer: The emissivity is greater for the case of lower density (Figure 33).

Now we show results for an ice layer without snow. For low thicknesses (up to approx. 30 cm) and lower frequencies we have found a strong dependency of the emissivity on the frequency. The emissivity oscillates as function of frequency (Figure 34). This is the same interference effect between the layer boundaries model as in our first model and arises

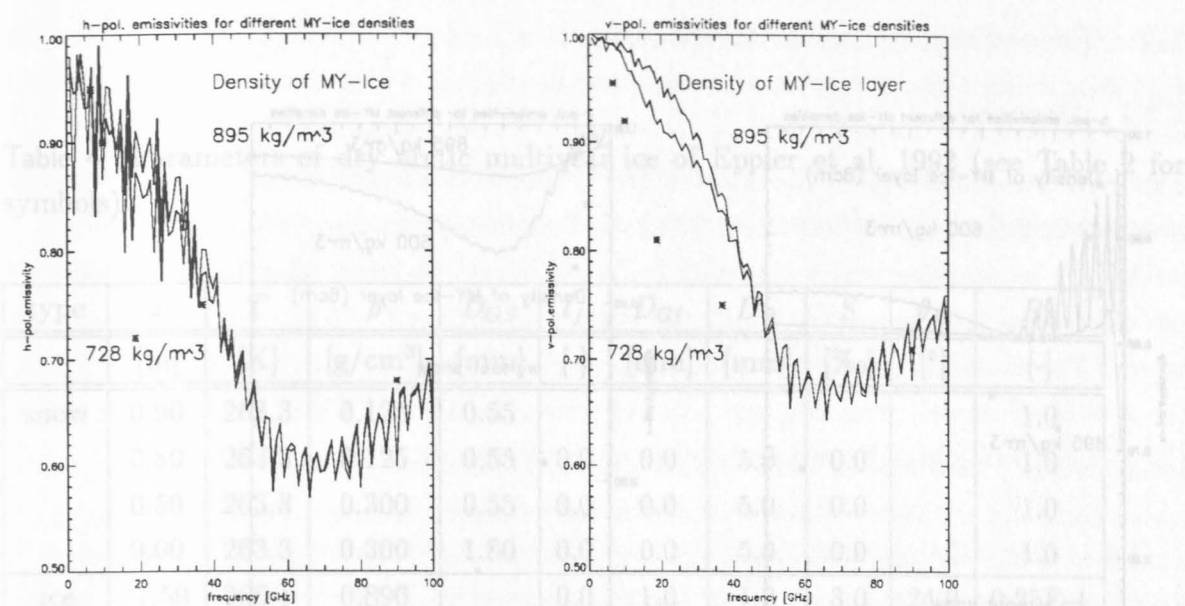


**Figure 32** Emissivities of sea-ice with snow and with different densities. Radiometric data are from CEAREX-experiment (Barents Sea) — Left: horizontally polarized emissivity — right: vertically polarized emissivity

from the plane parallel boundaries.

Due to the dielectric loss of the ice the oscillations disappear with increasing frequency and ice thickness (Figure 34). For greater thicknesses of the ice layer the emissivity does not depend on the layer thickness. The volume scattering for ice is negligible. In our third example we consider the case of greater volume scattering. To find a good parameterization for the ice model without knowing more details of the measurement we have used the two facts:

- The penetration depth depends on the frequency
- The emissivity depends on snow grain size and density

So we have found for the radiometric data of dry arctic multiyear ice of the table of Eppler (1992) the parametrization given in Table 4 The influence of the reflection at the boundaries is low for frequencies greater approx. 20 GHz. This is shown in Figure 35 and is due to the fact that we have assumed a thick snow layer with great volume scattering. To get low values for the emissity at high frequencies from the model we need snow or snow like layers.



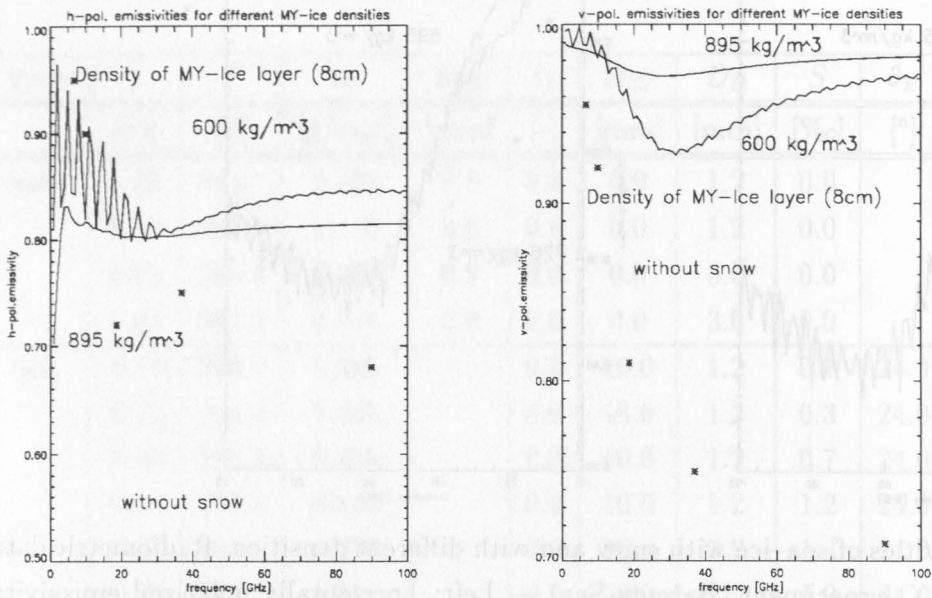


Figure 33 Emissivities of sea-ice without snow and with different densities. Radiometric data are from CEAREX-experiment (Barents sea) — Left: horizontal polarized emissivity — right: vertical polarized emissivity

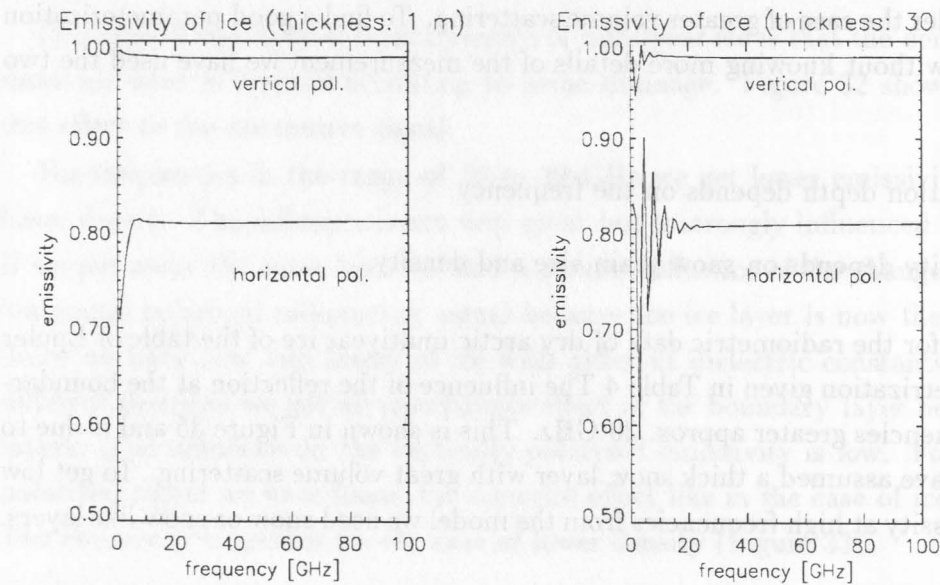


Figure 34 Emissivities of sea-ice without snow and with a thickness of one meter (left) and 30 cm (right).

Table 4 Parameters of dry arctic multiyear ice of Eppler et al. 1992 (see Table 2 for symbols).

type	$z$	$T$	$\rho$	$D_{GS}$	$l_f$	$D_{GI}$	$D_B$	$S$	$\theta_B$	$B_R$
	[m]	[K]	[g/cm <sup>3</sup> ]	[mm]	[-]	[mm]	[mm]	[‰]	[°]	[-]
snow	0.90	263.3	0.125	0.55						1.0
	0.80	263.3	0.125	0.55	0.0	0.0	5.0	0.0		1.0
	0.50	263.3	0.300	0.55	0.0	0.0	5.0	0.0		1.0
	0.00	263.3	0.300	1.80	0.0	0.0	5.0	0.0		1.0
ice	-1.50	266.1	0.890		0.0	1.0	1.2	3.0	24.0	0.25E-4
water		269.9	1.000		1.0			32.0		

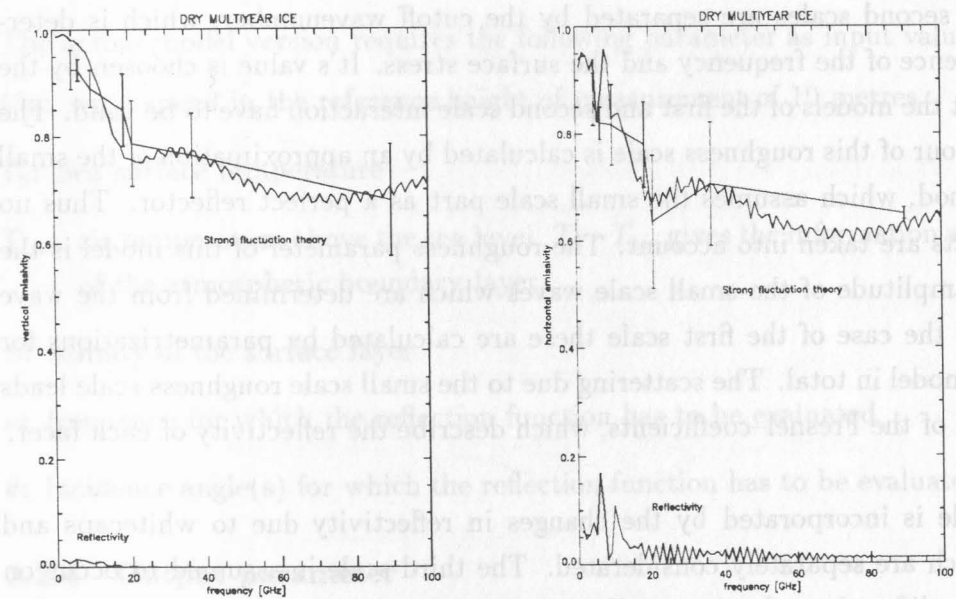


Figure 35 Comparison of the emissivities of dry arctic multiyear ice with the computed emissivities from the many layer strong fluctuation theory of Stogryn et al. Left: Vertical emissivity — Right: Horizontal emissivity. The parameters are given in Table 4.

## 3.2 Free–Ocean Surface Module

### 3.2.1 Description

The more scale model gives the opportunity to calculate the scattering matrix of a wind-roughened, foam-covered ocean surface based on first principles. The first scale is described by hydrodynamical waves with radius of curvature larger than the wavelength of the electromagnetic waves by which the surface is detected. These are mostly gravity waves. The formalism to calculate the scattering coefficients of such a surface is given by the *Kirchhoff*-model, assuming specular reflection on the inclined portions of the waves (facet model) weighted by the probability of the occurrence of the slopes.

Due to the statistical character of the approach of the *Kirchhoff*-model, the probability distribution function is expressed by the slope variances. These are calculated from the wave spectrum described by the model of Bjerkaas and Riedel (1979). The slope variances are determined in the three scale model by parameterizations calculated from the wave spectrum in dependence of friction velocity and frequency. The second scale is given by the short waves, which remain in the wave spectrum if the waves of the first scale are removed. These are typically the very short gravity waves and the capillary waves, depending on frequency.

The first and second scales are separated by the cutoff wavenumber, which is determined in dependence of the frequency and the surface stress. It's value is chosen by the requirement, that the models of the first and second scale interaction have to be valid. The scattering behaviour of this roughness scale is calculated by an approximation of the small perturbation method, which assumes the small scale part as a perfect reflector. Thus no polarization effects are taken into account. The roughness parameter of this model is the variance of the amplitude of the small scale waves which are determined from the wave spectrum. As in the case of the first scale these are calculated by parametrizations for efficiency of the model in total. The scattering due to the small scale roughness scale leads to a modification of the Fresnel-coefficients, which describe the reflectivity of each facet.

The third scale is incorporated by the changes in reflectivity due to whitecaps and foamstreaks, which are separately considered. The third scale is assumed to occur on each facet and modifies the reflection coefficient of the facet in such a way that it takes the form:

$$R_{mod} = R_r (1 - FC_{wc} - FC_{fs}) + R_{wc} FC_{wc} + R_{fs} FC_{fs}. \quad (56)$$

where  $R_{mod}$  denotes the effective reflection coefficient of the facet,  $R_r$  the reflection coefficient of the foam free part,  $R_{wc}$  the reflection coefficient of white caps, and  $R_{fs}$  the reflection coefficient of the foam streaks. A normalization in the integration procedure

of the first scale leads to an exact treatment of the mathematical problem. It shortens the computer time by a factor of eight in comparison to a facet model version with high resolution to come to the same accuracy in reflectivity. The reduction in reflectivity due to shadowing effects is incorporated. Multiple scattering is considered by an approximated and efficient approach, which takes the mainly geometrical effect of multiple scattering into account (Guissard et al. 1987).

### 3.2.2 Model Structure

The three scale model is implemented in the combined radiative transfer model as the submodule IAPOCE. It can be used alternatively to the modified specular reflection model of Wisler and Hollinger (1977) with the foam parametrization of Stogryn (1972) and foam cover of Monahan and O'Muircheartaigh (1986). The three scale model is written in FORTRAN-77 language. The flow chart (Fig. 36) shows the structure of the model. It is formulated in a number of subroutines. These make it easy to change and replace single codes of the model as the parametrizations to calculate the slope variances, the amplitude variances and the foam coverage as it will be necessary in the actual case of the combined model for the polar regions.

### 3.2.3 Input parameter

The actual model version requires the following parameter as input values

$U_{10}$ : wind speed in the reference height of measurement of 10 metres

$T_0$ : Sea surface temperature

$T_{air}$ : air temperature above the sea level.  $T_0 - T_{air}$  gives the information about the stability of the atmospheric boundary layer.

$S$ : salinity of the surface layer

$\nu$ : frequency for which the reflection function has to be evaluated

$\theta$ : incidence angle(s) for which the reflection function has to be evaluated

### 3.2.4 Output parameter

The model calculates the reflection function for the incoming and scattered zenith angles. This leads to a twodimensional scattering matrix for each polarization state  $\Gamma_H$  and  $\Gamma_V$ . The consideration of the azimuthal dependence of the scattering behaviour is possible and formulated in the model. The scattering problem is actually reduced to the two dimensional case in zenithal dependency by integrating (averaging) over the azimuthal direction. This shortens the computer time by a considerable amount.

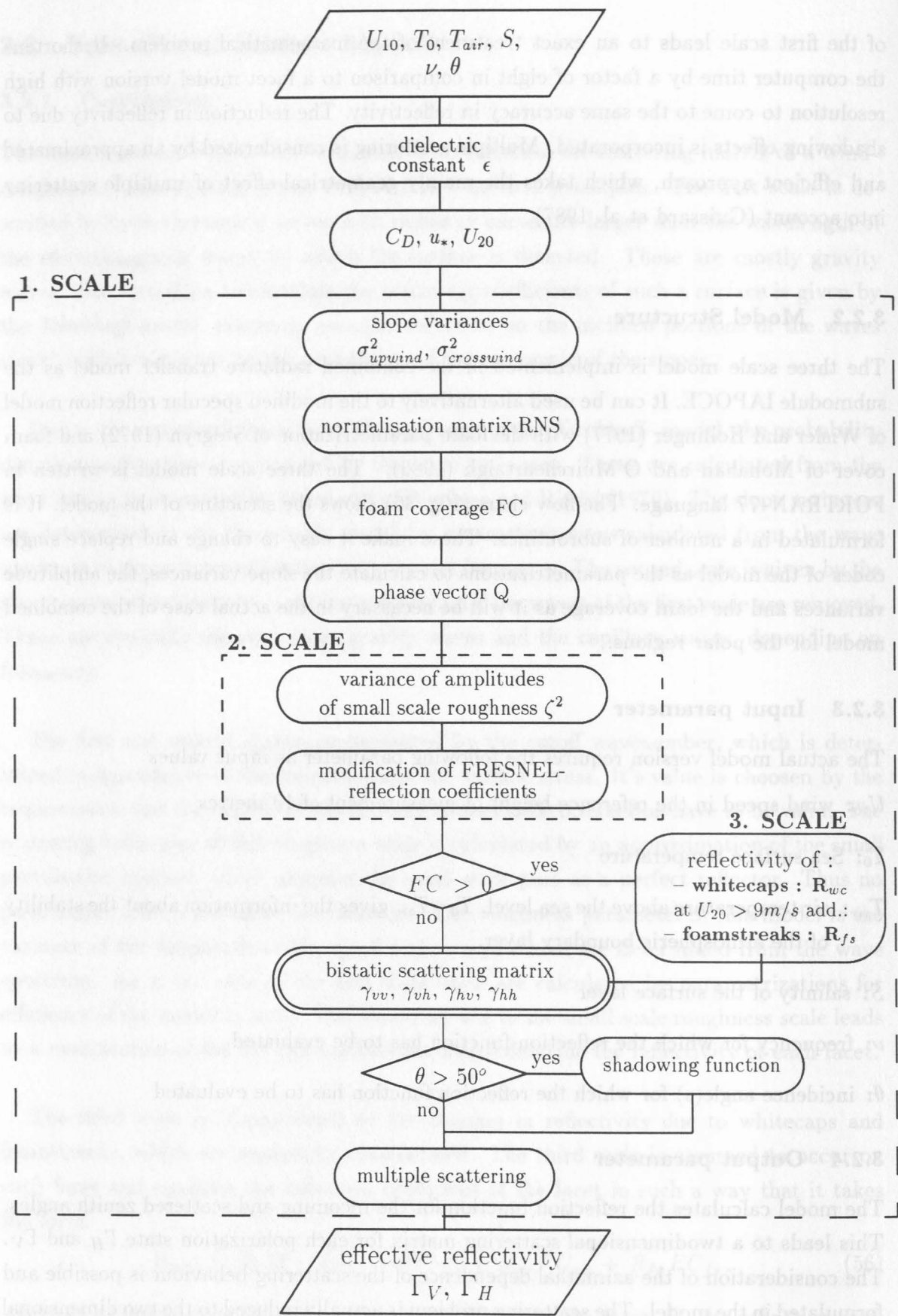


Figure 36 Flow chart of the 3-scale model



### 3.3 Atmospheric Module

#### 3.3.1 Selection of Code

The outcome of the model review is the recommendation to use either the Matrix Operator Method (MOM) or the Successive Order of Scattering Method (SOS) to numerically integrate the equation of radiation transfer. Coded versions of both methods are available at IfM-Kiel (Simmer 1994 for SOS, Liu and Ruprecht 1995 for MOM). It was finally decided to use SOS because of the following reasons:

- SOS is much faster and of equal accuracy compared to MOM for all atmospheric situations except heavy rainfall with extensive scattering. Computational efficiency, however, will be important.
- The SOS-code used at IfM is well documented and versions of the code have been distributed to and are in use at the Deutsche Wetterdienst, Alfred-Wegener-Institute Bremerhaven and at the Institute for Environmental Physics at the University of Bremen.
- The SOS-code has been programmed largely in a modular structure. This facilitates the restructuring of the code to fit into the overall modular scheme of the combined model to be developed.

#### 3.3.2 Successive Order Scattering Method

The Successive Order of Scattering method is based on the formal solution of the integro-differential radiative transfer equation (14) and is described e.g. in Goody and Yung (1989). This solution relates in an integral way the radiance in an arbitrary direction and at an arbitrary layer in the atmosphere directly to the complete radiance distribution in all directions and at all atmospheric layers.

The intensity  $L^\pm$  is described by a series of partial intensities  $L_n^\pm$

$$L^\pm(\delta, \mu, \varphi) = \sum_{n=1}^{\infty} L_n^\pm(\delta, \mu, \varphi), \quad (57)$$

where  $\pm$  denotes the upward (+) and downward (−) direction of the radiance and  $\mu$  is  $\cos \vartheta$ . For a plane-parallel atmosphere the partial intensities are given by

$$I_n^+(\delta, \mu, \varphi) = \frac{1}{\mu} \int J_n^+(\delta, \mu, \varphi) e^{-(\delta-\delta_0)/\mu} d\delta \quad (58)$$

$$I_n^-(\delta, \mu, \varphi) = \frac{1}{\mu} \int J_n^-(\delta, \mu, \varphi) e^{-(\delta_0-\delta)/\mu} d\delta. \quad (59)$$



The source function  $J_n^\pm$  includes the scattering phase function  $P$  and the primary source function  $\Sigma$

$$J_n^\pm(\delta, \mu, \varphi) = \frac{\omega_0}{4\pi} \int_0^{2\pi} \left[ \int_0^1 P(\delta, \pm\mu, \varphi, \mu', \varphi') L_{n-1}^+(\delta, \mu', \varphi') d\mu' + \int_0^1 P(\delta, \pm\mu, \varphi, -\mu', \varphi') L_{n-1}^-(\delta, \mu', \varphi') d\mu' \right] d\varphi' + \delta_{1n} \Sigma^\pm(\delta, \mu, \varphi), \quad (60)$$

where  $\delta_{1n}$  is the Kronecker symbol. These equations can be recursively solved with  $L_0^\pm = 0$ . The convergence of the series depends on the optical depth  $\delta$  and the single scattering albedo  $\omega_0$ .

The final solution is sought in an iterative manner:

1. Solve the radiative transfer equation without scattering ( $\omega_0 = 0$  or  $L_0^\pm = 0$ ). In case of absent hydrometeors this solution is the final one and no iteration is necessary. This will be the case for all atmospheric conditions without thick clouds.
2. Use the result of 1. as a first guess of the final radiance distribution for the right-hand side of the formal solution of the transfer equation and compute an improved guess.
3. Iterate 2. with the improved guess until the difference between the improved guess and the prior estimate is below a predefined value at all angles and all layer boundaries.

The  $n$ -th iteration can be interpreted as the contribution from photons scattered  $n$ -times: the first iteration corresponds to the photons scattered only once, the second iteration corresponds to the photons scattered twice, and so on. So the computation time is directly proportional to the number of scattering events necessary to be taken into account. It can be shown, that this solution is formally identical to the Monte-Carlo-Method (Liu and Simmer 1996).

In the context of microwave radiative transfer the SOS has been used first by Weinman and Guetter (1977) and Jung (1980). The code used at IfM has been developed by Simmer (1994) and includes the following upgrades and extensions to similar methods:

- The latest version (upgrades at irregular intervals) of gaseous absorption coefficients from Liebe (1981, 1985, Liebe and Layton 1987, Liebe 1992) is used.
- The code makes allowance for arbitrary anisotropic boundary conditions and boundary sources. In its current state the model is dedicated to oceanic applications (e.g. Karstens et al. 1994) and uses either the modified specular reflectance model by

Wisler and Hollinger (1977) or the Kirchhoff approximation of the wind-roughened ocean surface by a distribution of tangential planes coded according to Ulaby et al. (1986, p 1442 ff) with foam parameterizations by Stogryn (1972) and foam cover by Monahan and O'Muircheartaigh (1980).

- Arbitrary vertical distributions of atmospheric thermodynamic parameters and constituents are allowed. Hydrometeors can be specified by density or equivalent rain rate, phase, and size distribution parameters of the modified Gamma (Deirmendjian 1967, Willis 1984) or Marshall–Palmer size distributions (Marshall and Palmer 1948).
- Instead of a scalar phase function the code comprises the 2 by 2 phase matrix programmed according to Tsang et al. (1985). This is necessary for the correct solution of the radiative transfer equation (Liu and Simmer 1996).

### 3.3.3 Verification and Validation

The code has been successfully verified by comparison with other radiative transfer codes:

- Absorption and emission by the gaseous atmosphere through comparison with the results of the microwave intercomparison workshop held at the University of Maryland (Künzi et al. 1987).
- Effects of liquid and frozen hydrometeors based on the Rayleigh–phase function approximation by comparison with the results from Weinman and Guetter (1977).
- Atmospheric conditions from clear sky to heavy precipitation with overlapping profiles of liquid and frozen hydrometeors by comparison with the Eddington-based method by Kummerow (Kummerow and Giglio 1994) published in Burns et al. (1994)
- Atmospheric conditions from clear sky to heavy precipitation with overlapping profiles of liquid and frozen hydrometeors by comparison with the Matrix Operator Method (MOM) developed by Liu (Liu et al. 1991, Poetzsch–Heffter et al. 1994, Liu and Ruprecht 1995).

All comparisons showed differences of mostly less than 1 K. Larger differences occurred for the comparison with the Eddington method for heavily precipitating clouds especially when ice was included. A possible explanation is the restriction of the compared Eddington code to scalar phase functions.

The code has been validated by comparison with SSM/I measurements for clear sky cases only during the International Cirrus Experiment (ICE, Hennings et al. 1990). During the overpasses of the DMSP–F8 satellites radiosondes were launched from the research

vessel RV Poseidon and from the isle of Helgoland, where surface and cloud conditions were carefully monitored (Fuhrhop et al. 1990). For the cloud-free cases the atmospheric profiles and surface wind served as input for MWMOD. Systematic differences were found between 1 and 3 K for the low-frequency channels (19, 22, and 37 GHz) but differences up to 6 K for the 85 GHz channel for horizontal polarization (the vertical polarized channel was out of function). Recent comparisons with large sets of globally distributed radiosondes by Fuhrhop (1994, private communication) and Gäng, and Petty (1995, private communication) confirmed these differences within the range of uncertainty. A large part of the differences, especially for the 85 GHz channel, can be attributed to the ocean surface reflection model.

The code so far solves the radiative transfer equation for the zenith-dependent and azimuthally averaged radiance distributions, which justifies the restriction to linearly polarized radiation. Only spherical mono-phase particles are considered by the incorporated Mie-code. The extension to the full Stokes vector, the Müller scattering matrix and azimuthally dependent radiances would largely increase code size and computation time. So we did not include these characteristics.

We plan to incorporate non-spherical scatterers into the code, but not enough is known about their distributions and shapes. But atmospheric conditions which make their inclusion desirable (heavy precipitation) makes sea-ice retrieval largely impossible due to the low transmittance of the atmosphere.

## 3.4 Programme Structure of the Combined Model

### 3.4.1 Introduction

The individual models for the atmosphere, free ocean, and sea ice (discussed in the previous sections) have been combined into one model MWMOD. The code is programmed in FORTRAN. MWMOD computes for an arbitrary physical state of the atmosphere and the surface of the earth the radiance distribution at the top and bottom of the atmosphere in the microwave frequency range. A detailed model documentation is supplied with the source code of the model<sup>1</sup>.

The programme structure of MWMOD is closely related to the radiative transfer calculation. The equation of radiative transfer for the microwave frequency region, assuming a scatter free atmosphere and a specular reflecting surface, which gives the upward directed

---

<sup>1</sup>available from

<http://www.ifm.uni-kiel.de/me/research/Projekte/RemSens/SourceCodes/source.html>

brightness temperatures at the top of the atmosphere can be written as:

$$T_B = (1 - \Gamma) T_0 e^{-\delta_0/\mu} \quad (61.a)$$

$$+ \int_0^{\delta_0} T_a e^{-\delta/\mu} \frac{d\delta}{\mu} \quad (61.b)$$

$$+ \Gamma e^{-\delta_0/\mu} \int_0^{\delta_0} T_a e^{-(\delta_0-\delta)/\mu} \frac{d\delta}{\mu} \quad (61.c)$$

$$+ \Gamma T_{sp} e^{-2\delta_0/\mu} \quad (61.d)$$

with

$T_B$	brightness temperature at the top of the atmosphere
$\Gamma$	surface reflectivity
$\delta_0$	nadir optical depth of the total atmosphere
$\delta$	nadir optical depth from top of the atmosphere to specific height
$\mu$	cosine of zenith angle
$T_0$	temperature of surface
$T_a$	temperature of atmosphere
$T_{sp}$	temperature of space

The brightness temperature ( $T_B$ ) at top of the atmosphere is the sum of four contributions:

- the emission from the surface (61.a),
- the upward directed emission of the atmosphere (61.b),
- the downward directed emission of the atmosphere which is reflected at the surface (61.c), and
- the emission from space reflected at the surface (61.d).

The *emission from the surface* (61.a) in general is the strongest contributor. The surface emission ( $[1 - \Gamma] T_0$ ) is attenuated by the total atmosphere. The fraction reaching the top of atmosphere is given by the transmissivity  $\tau_0 (= e^{-\delta_0/\mu})$ . The nadir optical depth  $\delta$  is defined as the integral over the height  $z$  of the volume extinction coefficient  $\sigma_e$

$$\delta(z) = \int_z^\infty \sigma_e(z) dz \quad (62)$$

For the total optical depth  $\delta_0$  the integral is taken from  $z=0$  to  $z=\infty$ . For zenith angles  $\theta$  other than nadir the path length of the radiance has to be adjusted by  $1/\mu (=1/\cos \theta)$ . The surface reflectivity  $\Gamma$  is a function of zenith angle, frequency, polarization and other

physical parameters, e.g. temperature and salinity.  $\Gamma$  is computed from the bistatic reflection coefficients  $\gamma$  of the 3-scale ocean module and/or the sea ice module. The surface emission  $E_r$  as function of the zenith angle  $\theta$  is given by (Peake 1959)

$$\begin{aligned} E_r(\theta) &= \left(1 - \frac{1}{4\pi} \int [\gamma_{rr}(\theta', \theta) + \gamma_{tr}(\theta, \theta')] \sin \theta' d\theta'\right) T_0 \\ &= (1 - \Gamma) T_0, \end{aligned} \quad (63)$$

where denote  $r$  and  $t$  the polarization. The total surface emission is the with the sea ice concentration  $f$  weighted sum of the emission from sea ice and open water

$$E_{r,tot} = f E_{r,ice} + (1 - f) E_{r,ocean}. \quad (64)$$

The *upward emitted atmospheric radiation* is given by (61.b). An atmospheric layer with the air temperature  $T_a(\delta)$  (the optical depth  $\delta$  is used as the vertical coordinate) emits with  $T_a d\delta$ . This emission is attenuated by the atmosphere above, which is accounted by  $e^{-\delta/\mu}$ . Because this has to be considered for all atmospheric layers, an integration from the top of atmosphere ( $\delta=0$ ) to the surface ( $\delta=\delta_0$ ) is required.

Because the atmosphere also emits in downward direction, the *downward emitted radiance*, which is reflected at the surface upto the space (61.c), has to be taken into account. The downward directed emission from an atmospheric layer ( $=T_a d\delta$ ) is equal to that emitted in upward direction. However, we have to account for the attenuation from this layer down to the surface, which is done by  $e^{-(\delta_0-\delta)/\mu}$ . Thus the total downward emission of the atmosphere reaching the surface is given by the integral in (61.c). In the case of a specular reflecting surface the fraction of the upward reflected radiance is determined by the surface reflectivity  $\Gamma$ . Because the downward directed emission of the atmosphere  $T_a^\downarrow$  is a function of the zenith angle, the surface reflection  $R_r$  is given by

$$R_r = \frac{1}{4\pi} \int [\gamma_{rr}(\theta, \theta') T_{Ar}^\downarrow + \gamma_{rt}(\theta, \theta') T_{At}^\downarrow] \sin \theta d\theta. \quad (65)$$

The total surface reflection is the weighted sum of the sea ice and open ocean contributions as for the emission. On the path to the top of the atmosphere the reflected radiance again is attenuated by total atmosphere, which is contributed by  $e^{-\delta_0/\mu}$ .

The contribution of the *background radiation from space* is small, but not negligible (61.d). This radiance passes the atmosphere two times, first from space to the surface, and after reflection at the surface from the surface back to space. Thus the optical depth has been doubled for the transmission term.

The combined model is made up of 3 modules (see next section), each of them is responsible for a specific task. The computation of the equation of radiative transfer is

done by the third module *RADTRA* of *MWMOD*. To perform this task the module has to know all necessary parameters: the temperatures, surface reflectivities and the optical depth. The surface reflectivities are computed from the bistatic reflection coefficients and the optical depth is given by the absorption and scatter coefficients. This is done in the second module *IAPGEN*. To calculate these parameters, environmental quantities, such as temperatures, salinity, and densities are necessary. These parameters are generated by the first module *ENVGEN*. To summarize it follows that we have to

1. Generate the physical environment for the atmosphere, ocean and sea ice
2. Compute the interaction parameter from the environmental data
3. Use the interaction parameter to solve the equation of radiative transfer.

### 3.4.2 The General Layout of *MWMOD*

The general layout of the programme structure is given in Fig. 37. *MWMOD* consists of three modules (*ENVGEN*, *IAPGEN*, and *RADTRA*). The modules *ENVGEN* and *IAPGEN* are made up of sub-modules which generate the individual quantities for each environment: *ENVATM* and *IAPATM* for the atmosphere, *ENVOCE* and *IAPOCE* for the open ocean, and *ENVICE* and *IAPICE* for the sea ice.

The data exchange between the modules is handled by unformatted FORTRAN files with the extension *.bin* (formatted files can also be created). The model is controlled by parameters, which are defined in the parameter control file *runpar.par*. Another control file is *files.*, which defines almost all filenames used by the model (filenames for external environmental data are defined in *runpar.par*). The specification of the filenames in *files.* is necessary by two reasons:

- pathname specifications depend on the operating system (we like to be independent)
- to change the filenames for various reasons, e.g. to overcome disk storage problems or saving the data for different simulation experiments, without to recompile the model.

#### 3.4.2.1 Generation of the Environment

The first task for *MWMOD* is to define the physical environments, which describe the situation under investigation. Because we deal with three environments, the parameters are created by sub-modules: *ENVATM* for the atmosphere, *ENVOCE* for the open ocean, and *ENVICE* for the sea ice. The atmosphere is described by profiles of temperature and humidity as function of height. Additionally hydrometeors (clouds, rain, ...) can be



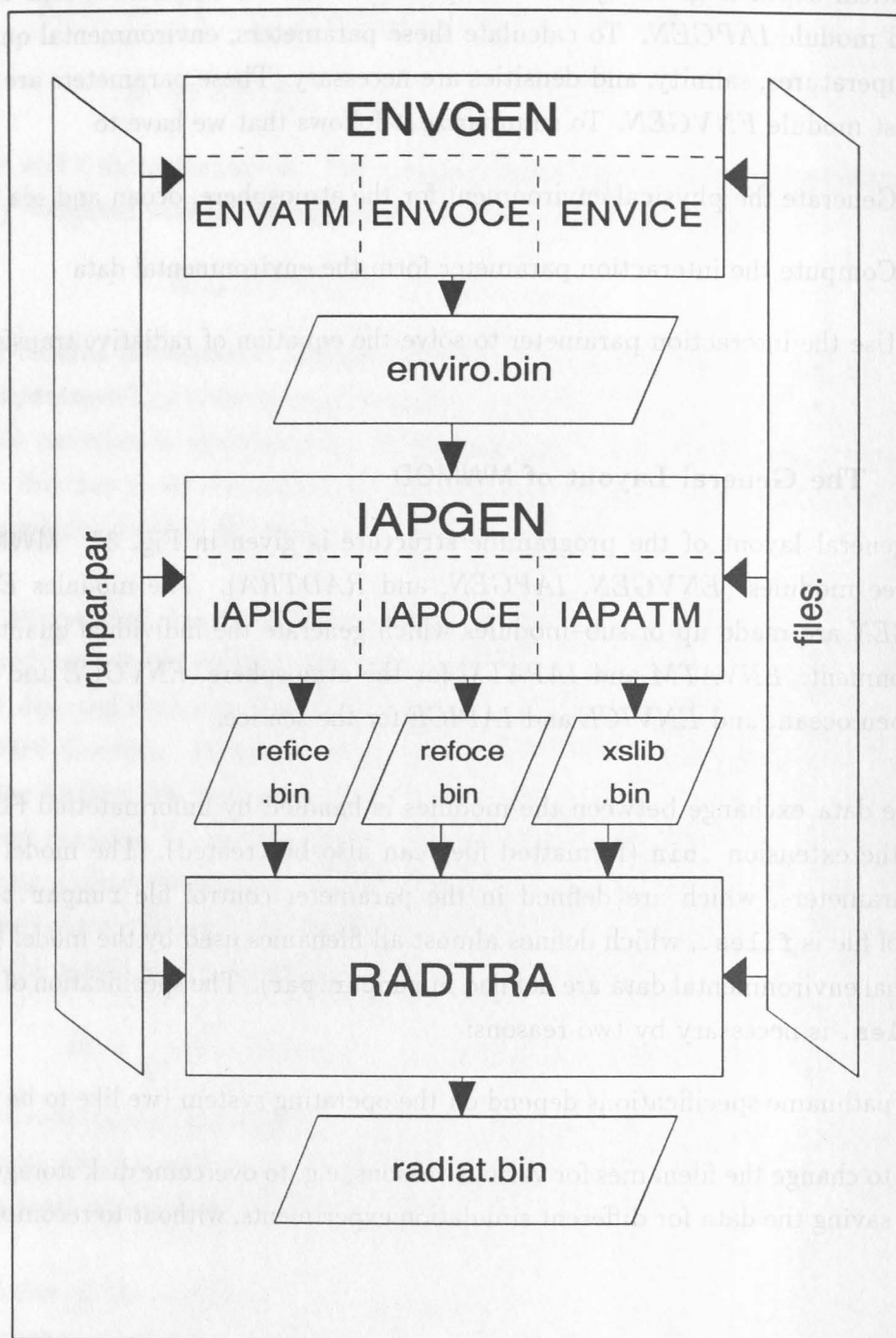


Figure 37 General Layout of the Combined Model

introduced. To compute the ocean surface reflectivity the sea surface temperature, salinity and wind speed are required. Actually the surface roughness is the important parameter, but the wind speed is a measure of it. The sea ice reflectivity depends on the sea ice profile, which is described by many parameter, including temperature, density, salinity and so on. The sea ice profile also includes data of overlaying snow. All sub-modules established the parameters according to the control parameter in `runpar.par`. The environmental data generated by all sub-modules is written into the unformatted file `enviro.bin` for later use by the module *IAPGEN*.

### 3.4.2.2 Generation of the Interaction Parameters

The interaction parameters described the interaction between a medium and an electromagnetic wave. These are the extinction coefficients and phase functions for the atmosphere, and the surface reflectivities for the ocean and sea ice surfaces. The generation of the interaction parameters is performed with the module *IAPGEN*. Because each environment has its own type of interaction parameters and an individual way to compute them, this is done in the three sub-modules *IAPATM*, *IAPOCE*, and *IAPICE*. The results are stored in three unformatted files (of course you can create formatted versions). The surface reflection parameters are written into `refice.bin` (sea ice) and `refoce.bin` (open ocean). The atmospheric absorption and scatter coefficients are saved into `xslib.bin`. The parameters for the scattering phase function are written into `phasef.bin` (not shown in Fig. 37).

### 3.4.2.3 Radiative Transfer

After the execution of *IAPGEN* all parameters required to solve the equation of radiative transfer have been generated. The last task, solving the radiative transfer equation, is done in module *RADTRA*. The final brightness temperatures are stored into the file `radiat.bin` (unformatted form). An example of the formatted form `radiat.dat` is given in Fig. 38. The upper part lists the values of the relevant control parameter. This listing is followed by an input data description for each environment. Following these statistics the simulated brightness temperatures are given for each viewing angle and frequency. The upper part of the brightness temperature listing gives the values for a space-borne downward looking radiometer. The second part lists the brightness temperatures simulated for an upward looking radiometer at the surface. The brightness temperatures listings are grouped into blocks for viewing angles. The frequency is given GHz.  $\Delta$  is the total nadir optical depth. RV and RH gives the equivalent surface reflectivity for the vertical and horizontal polarization. The equivalent surface reflectivity is defined as the reflectivity for a specular reflecting surface. The actual reflection model used depends on the control parameter settings in `runpar.par`. The simulated brightness temperatures are in Kelvin and denoted by R.T.(V) for the vertical and R.T.(H) for the horizontal polarization.

Run Parameters: ISCAT=1 IRAL =0 IGAAB=0 IPHA =2 ICUR =0 IOPT=-1 IWFT=11									
IREF =3 EPSIL=0 IFRE= 1 NFR= 1 IANG = 3 NANG= 6 NZL= 70									
NZLC= 72 NLICE= 13 ITHYST= 0 IPHMAX= 0 ITHMAX= 0 ICOV= 2									
Atmosphere: ATMOS= 1 MODEL= 1 IBNDL= 0 ITOP = 0 HYDRO= 0 1 IMESH= 0									
IFOAM= 4 ITEM = 0 IWV = 0 TWV= 1.00 TO2= 1.00 THY= 1.00									
Ocean Quantities : SST : 288.00 K Sa : 33.00 Prom. WND : 14.00 m/s									
Sea Ice Quantities									
Ice Cover : 70. %									
Emission Temperatures [K] (v/h) : 263.5 263.1 K									
Atmosphere quantities									
PLL :1013.00 hPa TLL : 14.85 C RHLL : 46.38 %									
W : 14.64 kg/m2 W850 : 6.80 kg/m2 WS85 : 6.42 kg/m2									
WM : 29.45 kg/m2 W850M: 14.31 kg/m2 WS85M: 13.53 kg/m2									
TM850: 10.42 C T850 : 5.67 C DT850: -6.31 K/km									
TMS85: 10.76 C TS85 : 6.41 C DTS85: -6.26 K/km									
Hydro Type LWP kg/m2 LWmax g/m3 Bottom-Top km Top.T C RR mm/h RRI mm/h									
water cloud 0.0000 0.0000 0.000- 0.000 -999.99 0.00 0.00									
ice cloud 0.0000 0.0000 0.000- 0.000 -999.99 0.00 0.00									
rain 1.2307 0.6153 3.000- 5.000 -17.15 0.00 10.00									
hail 0.0000 0.0000 0.000- 0.000 -999.99 0.00 0.00									
snow 1.2307 0.6153 5.000- 7.000 -30.15 0.00 10.00									
Upward at the Top of the Atmosphere									
1-th angle , 11.0 Degree									
# Frequency Delta RV R.T.(V) RH R.T.(H)									
1 18.00000 0.416 0.242 230.146 0.238 230.029									
:									
Downward at the Bottom of the Atmosphere									
1-th angle , 11.0 Degree									
# Frequency Delta RV R.T.(V) RH R.T.(H)									
1 18.00000 0.416 0.242 83.398 0.238 83.358									

Figure 38 Listing of simulation results in radiat.dat.

## 4 Model Validation

### 4.1 Review of Test Cases

The validation of radiative transfer models can be fulfilled by means of existing radiometric measurements and co-located in-situ observations of all variables affecting the radiative transport in the ice-atmosphere system. With respect to the MIMR instrument the most useful radiometric system to test the radiative transfer model would be the Special Sensor Microwave/Imager (SSM/I), being flown as part of the U. S. Defense Meteorological Satellite Program. The SSM/I measures the radiation at four frequencies between 19 and 86 GHz at vertical and horizontal polarization. The instrument is continuously calibrated allowing the computation of brightness temperatures. Radiosonde measurements together with in-situ observations of surface meteorological and cryospheric variables as obtained from field campaigns can be entered into a radiative transfer model to yield a calculated set of brightness temperatures that can be matched and compared with the satellite measurements co-located with the in-situ observations. However, this task is not as easy as it appears at a first glance because the sea-ice coverage within the footprint of a SSM/I pixel rarely reaches 100%. The estimation of the sea ice concentration often is difficult, e.g. from AVHRR images it is limited to cloud free scenes. The validation of the ice-water-atmosphere model is best performed by first independently verifying the combined water-atmosphere model over the open ocean in an area close to the ice edge and finally to check the model consisting of three components in a sea-ice area.

Following the discussion above the validation with data from two Arctic campaigns is proposed which have been carried out under different meteorological situations, namely, the ARKTIS'88 and ARKTIS'93 experiments which were both initiated and directed by the Sonderforschungsbereich 318 of the Deutsche Forschungsgemeinschaft entitled 'Climatically relevant processes in the system ocean-atmosphere-cryosphere', established at the Universität Hamburg. Both campaigns took place in the Fram Strait and the Greenland Sea. They were supported by research vessels, aircraft, ice-floe stations, ice-drift buoys and satellites. During both experiments an ice station was set up on an ice floe in the pack ice at a distance of about 100 km from the marginal ice zone. The ice-floe stations were hosted by the research ice breaker R/V Polarstern from which radiosondes were launched four times per day. Another research vessel, the R/V Valdivia was operating in the open water of the Greenland Sea, also performing frequent radiosonde launches and measuring surface meteorological parameters. In the ARKTIS'93 experiment a third vessel, the R/V Prof. Multanovsky, was included with measurements in the Greenland Sea close to the ice edge. The aircraft were operated from the airfield in Longyearbyen on Spitsbergen and several of the flights were coordinated with the measurements near the ice floes and with those made in the open sea.



#### 4.1.1 ARKTIS'88

This experiment was carried out from 4 May to 2 July 1988. The ice-floe station was drifting near  $80.5^{\circ}\text{N}$ ,  $10^{\circ}\text{W}$  in the pack ice and was accompanied by the Polarstern. Besides the standard meteorological surface and upper-air observations which are of relevance here a temperature chain consisting of 49 thermometers 0.1 m apart was measuring the temperature profile through the ice. Two sensors remained above the snow surface and a number of thermometers extended below the ice. The temporal sampling interval for these ice-temperature measurements was one hour. Analyses of the measurements revealed that sensors 3 to 28 were in snow or ice and that the temperature variance is an excellent indicator of the ice/snow boundary. The total ice and snow thicknesses were 2.17 m and 0.47 m, respectively, with a variation in ice thickness during the onset of the melting period. This information will be a valuable input to the ice model to be developed. Additionally, the snow surface was measured via infrared radiometry. Cloud microphysical parameters are available for few cases from research flights covering the area around the ice floe. The ice-floe station, named SAFE<sup>2</sup> Island, was occupied from 4 to 23 May 1988 having 'average appearance with respect to surface roughness, and thickness' (Hoeber 1989). The floe had a diameter of about 2 km and a thickness of 2.5 to 3 m. A part of the flow showed a reduced thickness of only 1.5 m which, as seen during the campaign, was a separate ice floe glued to the thicker part. Minor ridges indicated the join which, however, held only until 9 May where the floe broke into two parts again. The station was located about 100 km from the ice edge. Apart from the minor ridges indicating the join of the two floes no other ridges were seen. The appearance as seen from photographs is a rather smooth snow cover. An inspection of the vicinity of the ice camp with a helicopter showed all kinds of different ice types and open water, too. After 23 May 1988 the instruments were partly left on the floe and data were transmitted via ARGOS until 2 July 1988.

The Valdivia was operating near  $79.5^{\circ}\text{N}$ ,  $8^{\circ}\text{E}$ , radiosonde launches were done six times per day and accompanied by continuous observation of surface meteorological variables as well as hourly cloud observations. As with the ice-floe station several research flights were coordinated with the measurements on board the Valdivia. A rendezvous of Valdivia and Polarstern near the end of the campaign was used to intercompare surface and upper air observations.

The meteorological situations covered by the ARKTIS'88 experiment were quite heterogeneously distributed. Northerly off-ice flow as well as on-ice flow conditions occurred with different cloud characteristics. Clear-sky conditions, which are preferred robust reference cases for the use with radiative transfer simulations, are also covered by the experiment.

---

<sup>2</sup>Spring Arctic Floe Experiment

An overview about the sea-ice conditions and distribution in the vicinity of the ice floe is obtained by imagery of the AVHRR (Advanced Very High Resolution Radiometer) under clear-sky conditions. This information will be used to determine the fractional ice coverage, a final parameter that is needed for the simulations. The experiment design and the field phase have been described by Brümmer (1989). The data are archived at the Universität Hamburg and are available for the proposed study.

#### 4.1.2 ARKTIS'93

Unlike the ARKTIS'88 campaign this experiment was a winter campaign with extreme temperatures for the operation of a research vessel in the pack ice. The experiment took place from 1 to 25 March 1993, characterized by Arctic cold-air outbreaks which left the air temperature at the ice-floe station as low as  $-40^{\circ}\text{C}$ . Consequently, the instrumental equipment was measuring at its limits. The ice floe which was chosen drifted near  $81^{\circ}\text{N}$ ,  $5^{\circ}\text{W}$  about 50 to 100 km inside the Arctic sea ice. While the ice floe itself consisted of multi-year ice it was surrounded by ice-free water, young, and new ice on leads. Figure 39 shows the configuration of the ice station where single numbers indicate the positions of different instruments. Also indicated is the distribution of ridges, classified in small ones (height  $< 1$  m) and larger ones (height  $> 1$  m), those in the NW corner were the most prominent ones being higher than 2 m. As during the previous campaign the snow and ice temperatures were measured radiometrically as well as by a chain of thermometers lowered into the ice as described above. Other than in the previous campaign the chain was equipped with only 20 thermometers spaced at intervals of 30 cm. Hourly meteorological surface observations complete the set of surface measurements to be entered into the radiative transfer model. Radiosonde ascents were taken on board the R/V Polarstern operating close to the floe station every six hours. Research flights were carried out to measure cloud microphysical parameters.

In the open water of the Greenland Sea two research vessels, the Valdivia and the Russian ship R/V Prof. Multanovsky were in charge for radiosoundings, surface observations, and oceanographic measurements. The vessels were located near  $73^{\circ}\text{N}$ ,  $10^{\circ}\text{E}$  (Valdivia) and  $75^{\circ}\text{N}$ ,  $3^{\circ}\text{W}$  (Prof. Multanovsky). Details of the experiment are described in a field phase report (Brümmer 1993).

During the campaign the ERS-1 Synthetic Aperture Radar (SAR) instrument was switched on and delivered images of the ice surface at the station every three days. These images together with AVHRR imagery under cloud-free conditions will fully characterize the fractional ice coverage at the floe station during the experiment. The SAR as well as the AVHRR images are archived at the Universität Hamburg and at the Max-Planck-Institut für Meteorologie, they can be accessed for the use within this study.





Table 5 Summary of test cases selected for model validation

Case No.	Date	Time UT	Location	Characterization	Radiosonde Launches	SSM/I Passages
1	2 March 93	8-16	4.4°E, 68.6°N	ice-free ocean, partly cloud-free sky	10:29	11:08 12:48
2	14 March 93	0-10	5.4°E, 81.1°N	ice, low cloud fraction	04:33 10:26	08:32 10:13
3	16 March 93	8-16	5.1°E, 80.9°N	ice, overcast sky	04:18 10:29 16:28	08:07 09:48 11:28 13:09 16:32
4	18 March 93	11-17	5.0°E, 80.6°N	ice, low fraction of mid and high-level clouds	04:29 10:17 16:26	09:22 11:03 12:43 14:24 16:05
5	13 May 88 14 May 88	20-4	4.4°E, 80.7°N	ice, overcast sky	20:00 23:50 03:50	21:30 23:20
6	25 May 88	0-8	0.3°E, 80.2°N	ice, overcast sky	00:00 03:50 08:00	03:34 05:16

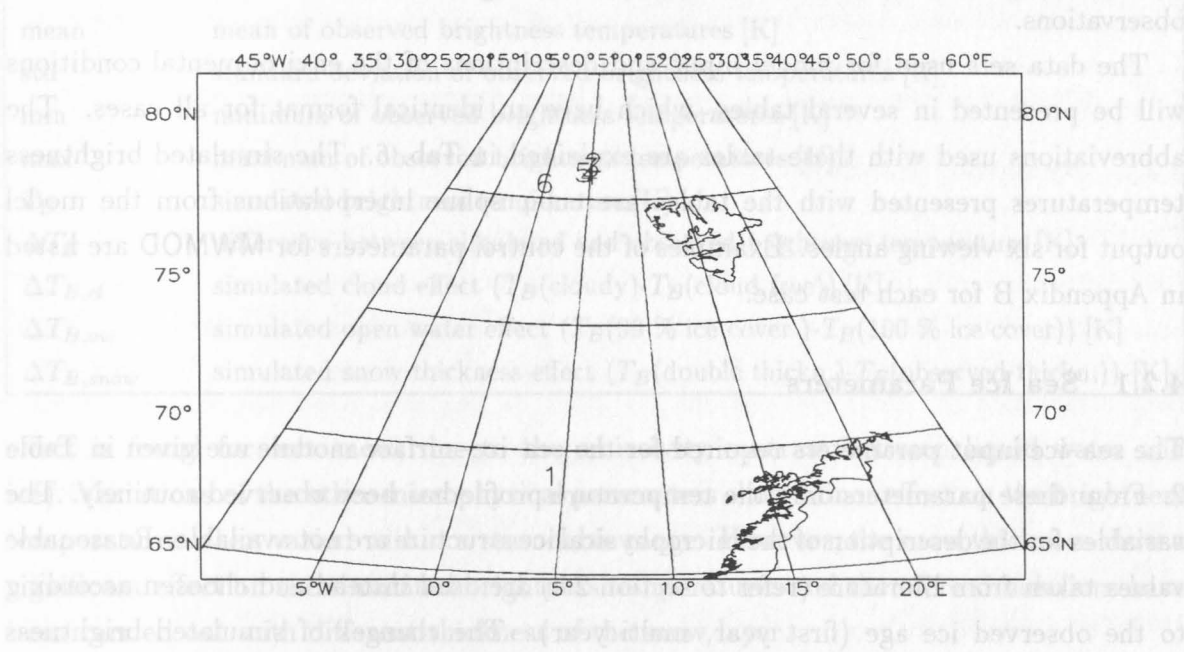


Figure 40 Locations of test cases indicated by numbers.

## 4.2 Ground Truth Requirements

To validate the combined microwave model, brightness temperatures are simulated according to the observed synoptic situation and are compared to observed SSM/I data. For the evaluation it is not expected to find an exact agreement between observed and simulated brightness temperatures. Differences in the order of a few Kelvin have to be expected, which may originate from an insufficient simulation or SSM/I instrument errors, as well as scene inhomogeneities, because the ground truth observations are point measurements, while the SSM/I observations are areal integrated. To reduce possible effects of geolocation errors of the SSM/I pixels, as well as to minimize the influence of horizontal inhomogeneities of the scene, the 10 nearest SSM/I observations (with respect to the lower frequency channels) are averaged. Since the footprint size of the SSM/I channels differ, the simulated brightness temperatures are also compared to restored SSM/I observations, i.e. resolution-unified brightness temperatures (see Appendix A).

The general strategy for the evaluation is to simulate brightness temperatures for varying environmental conditions (e.g. cloud free, cloudy, partially ice covered, ...) according to the synoptic observations. From these simulations the effect of changes of environmental conditions are derived and expressed by the sensitivity of the brightness temperatures to a certain parameter. This allows an estimation of the errors introduced by unknown parameter values (see below). However, it is not the task to retrieve the values for the unknown parameters. The validation will be considered to be successful, if the simulated brightness temperatures are close to the observed ones. The interpretation of 'close' depends on the synoptic conditions observed. The standard deviations of the observed brightness temperatures, as well as the estimated sensitivities have to be related to the synoptic observations.

The data sets used for model input and descriptions of the environmental conditions will be presented in several tables, which have an identical format for all cases. The abbreviations used with these tables are explained in Tab. 6. The simulated brightness temperatures presented with the tables are cubic spline interpolations from the model output for six viewing angles. Examples of the control parameters for MWMOD are listed in Appendix B for each test case.

### 4.2.1 Sea Ice Parameters

The sea-ice input parameters required for the sea-ice-surface module are given in Table 2. From these parameters only the temperature profile has been observed routinely. The variables for the description of the microphysical ice structure are not available. Reasonable values taken from literature (refer to section 2.6) are used instead and chosen according to the observed ice age (first year, multi year). The changes of simulated brightness temperatures due to the variation of the unknown parameters has been investigated for each test case to estimate the importance of a single parameter. The most pronounced

Table 6 Abbreviations used with tables for validation results.

Abbreviation	Meaning
<b>synoptic observations:</b>	
$T_a$	air temperature
$T_0$	sea surface temperature
cloud	cloud observation according to WMO code $NN_lC_lC_mC_h$ with:
N	total cloud cover
$N_l$	cloud cover of $C_l$ or $C_m$
$C_l$	cloud type of lower troposphere
$C_m$	cloud type of middle troposphere
$C_h$	cloud type of upper troposphere
PWC	precipitable water = vertically integrated water vapor amount
$\Delta T_{ice-snow}$	temperature difference between upper snow and upper ice layer
<b>sea ice input parameters:</b>	
$z$	depth of ice layer [m]
$T_i$	temperature of ice or snow [K]
$\rho$	density of ice or snow [ $g\ cm^{-3}$ ]
$D_{GS}$	diameter of snow grains [mm]
$l_f$	free water fraction
$D_{GI}$	diameter of ice grains [mm]
$D_B$	diameter of air bubbles [mm]
$S$	bulk salinity [‰]
$\theta_B$	mean tilt angle of brine pockets [deg]
$B_R$	brine pocket elongation (square of ratio of length and radius of brine cells)
<b>statistics of observed and simulated brightness temperatures</b>	
mean	mean of observed brightness temperatures [K]
std	standard deviation of observed brightness temperatures [K]
min	minimum of observed brightness temperatures [K]
max	maximum of observed brightness temperatures [K]
$T_B$	simulated brightness temperature [K]
$\Delta T_B$	difference between simulated and observed brightness temperature [K]
$\Delta T_{B,cl}$	simulated cloud effect ( $T_B(\text{cloudy}) - T_B(\text{cloud free})$ ) [K]
$\Delta T_{B,ow}$	simulated open water effect ( $T_B(99\ \% \text{ ice cover}) - T_B(100\ \% \text{ ice cover})$ ) [K]
$\Delta T_{B,snow}$	simulated snow thickness effect ( $T_B(\text{double thickn.}) - T_B(\text{observed thickn.})$ ) [K]

effect is found for wet snow, due to the emissivity contrast between liquid water and ice). Variations of the other microphysical parameters show minor effect on the brightness temperatures when varied within a reasonable range. However, the snow thickness show a significant effect on the simulated brightness temperatures and therefore simulations have been carried out with different thickness of the snow layer. The most prominent signal on the brightness temperatures arises from the amount of sea-ice concentration. Besides the AVHRR images and aircraft flights, the NASA sea ice



algorithm (Cavalieri 1992) has been applied to infer a reasonable sea-ice concentration from the SSM/I observations.

#### 4.2.2 Atmospheric Parameters

The atmospheric parameters (temperature and humidity) are taken from radiosonde measurements launched at test case sites close to SSM/I overpasses. Cloud microphysical parameters have been measured on several research flights during both campaigns, ARKTIS'88 and ARKTIS'93. Very few of them approached the ice-floe stations. The Falcon-20 of DLR which participated in both experiment was equipped with instruments to measure temperature, humidity, the wind vector as well as liquid-water density and cloud-droplet distribution and radiation fluxes. An analysis of the liquid-water measurements shows that even in stratocumulus clouds the variability of the liquid-water content and of the size distribution is immense and will hardly represent an areal average of the SSM/I's field of view. On a flight mission to the ice-floe station on 18 May 1988 the cloud liquid-water density of a stratocumulus varied between 0 and 2 g/m<sup>3</sup> while the mean droplet diameter varied between 0 and 60  $\mu\text{m}$  with a standard deviation of 350  $\mu\text{m}$ . Therefore, the cloud parameters are included according to known cloud models into the atmospheric profiles where the moisture profiles and the surface observations indicate clouds.

#### 4.2.3 Open Ocean Parameters

The required input parameters (sea surface temperature and wind speed) for the open-ocean surface module are taken from the station observations. The salinity is assumed to be constant with 33 ‰ for any test case.

### 4.3 Case 1: Free ocean, partly clear atmosphere, winter

#### 4.3.1 Synoptic Situation

The first situation chosen is a partly cloud-free scene in the Norwegian Sea on 2 March 1993 between 8 and 16 UT where the R/V Polarstern was steaming in the ice-free ocean near 4.4°E, 68.6°N towards the Greenland Sea, in the warm sector of a cyclone centered at Svalbard. Table 7 summarizes the synoptic data use for the simulations. Unfortunately,

**Table 7** Synoptic observations for case 1 (2 March 1993).

date : 2.3.1993	position : 4.4° E / 68.6° N	
SSM/I overpass : 12:48 UT	radiosonde launch : 10:29 UT	synop : 13 UT
pressure : 1016.0 hPa	$T_a$ : 4.7 °C	humidity : 98 %
wind speed : 17.6 m/s	$T_0$ : 5.0 °C	cloud : —
wind dir. : 221 °	PWC : 15.1 kg m <sup>-2</sup>	$\Delta T_{ice-snow}$ : —

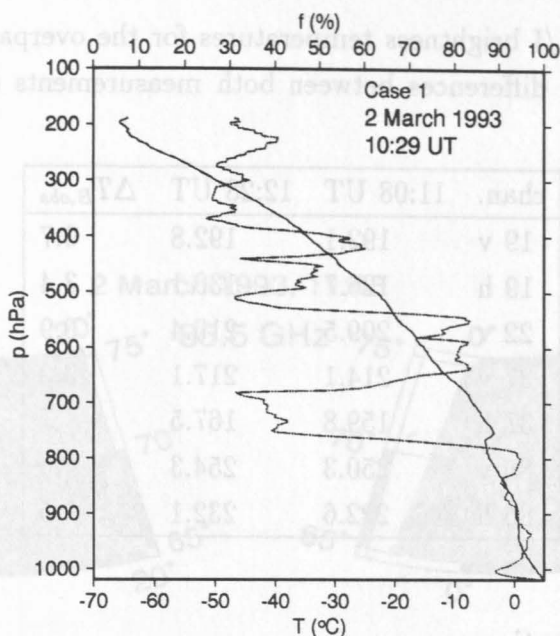


**Figure 41** Temperature (contiguous) and relative humidity (dotted) profiles for case 1; given time is launch time.

cloud observations have not been performed during this day. Therefore, AVHRR imagery as obtained from the NOAA-11 satellite has been analysed in order to study the cloud situation. The satellite image at 12:45 UT indicates a field of low stratiform clouds about 200 km northwest of the ship's position. This is also seen in the SSM/I 85 GHz vertically polarized brightness-temperature field showing temperature differences of 10 K between cloud-free and cloudy areas (Figs. 42 and 43). Hence, the cloud-free portion of the atmosphere can easily be separated. The prevailing wind direction is southwest, the wind speed is close to 18 m/s during this day. The surface air temperature varied between 4.3 and 5.0  $^{\circ}\text{C}$ , while the sea surface temperature dropped from 6.0  $^{\circ}\text{C}$  at 8 UT to 5.0  $^{\circ}\text{C}$  at 13 UT with a subsequent rise to 5.6  $^{\circ}\text{C}$  at 16 UT.

#### 4.3.2 Atmospheric Parameters

One radiosonde has been launched at 10:29 UT on this day (Fig. 41) showing a small temperature inversion at 770 hPa that separates high humidities (between 90 and 100%) in the lower troposphere from a dryer level between 770 and 690 hPa with only 35% relative humidity. Aloft, another moist layer with relative humidities up to 80% is seen between about 630 and 550 hPa. The tropopause is situated at 197 hPa with a temperature of -65.7  $^{\circ}\text{C}$ , indicating that the ship has not yet reached the arctic atmosphere. The SSM/I passages covering the area around the Polarstern have been at 1:08 and 12:48 UT. It should be noted that here and henceforth all humidity values refer to saturation over liquid water.



**Table 8** Averaged SSM/I brightness temperatures for the overpasses at 11:08 UT and 12:48 UT (case 1), and differences between both measurements ( $\Delta T_{B,obs}$ ). Values are given in Kelvin.

chan.	11:08 UT	12:28 UT	$\Delta T_{B,obs}$
19 v	192.1	192.8	0.7
19 h	126.7	130.1	3.4
22 v	209.5	210.4	0.9
37 v	214.1	217.1	3.0
37 h	159.8	167.5	7.7
85 v	250.3	254.3	4.0
85 h	222.6	232.1	9.5

4.3.3 SSM/I Observations

The images of the two SSM/I passages at 11:08 and 12:48 UT (Figs. 42 and 43) show that the cloud-free area surrounding the Polarstern is quite small and that a careful selection of the SSM/I soundings for the validation is indicated. The averaged SSM/I brightness temperatures of the individual overpasses around the ship position differ by several Kelvin depending on the SSM/I channel (Tab. 8). Particularly for 37 and 85 GHz horizontal polarization the differences are very high with 7.7 K and 9.5 K, respectively. Because the observed wind speed is nearly constant during the successive overpasses, these differences may be caused by changes in cloudiness. Both channels also exhibit large horizontal gradients at both overpass times (Figs. 44 and 45 for 12:48 UT), suggesting that the cloudiness is highly variable both in space and time.

4.3.4 Validation

The statistics of the observed SSM/I brightness temperatures at 12:48 UT and simulated brightness temperatures using the 3- scale model are shown in Tab. 9. Brightness temperatures assuming a cloud free atmosphere and a surface wind speed of 18 m/s are calculated with simulation 1. While the differences between the simulation and observation are small for the 22 GHz, 37 GHz channels, and 85 GHz vertical polarization, relatively large deviations are found for the 19 GHz channels, and 85 GHz horizontal polarization. To deduce a wind effect on the brightness temperatures, a cloud-free atmosphere has been simulated with a surface wind speed of 20 m/s (simulation 2). The estimated wind effect related to a change of 1 m/s ( $\Delta T_{B,wind}$ ) depends on polarization and frequency. For the horizontally polarized channels the effect is about twice in magnitude than for the corresponding vertically polarized channels. Moreover, the wind effect is largest for 37 and 85 GHz horizontal polarization. Simulations for a wind speed of 16 and 19 m/s give nearly the same wind effect (normalized to a 1 m/s change). Thus a wind speed error is at first order a linear

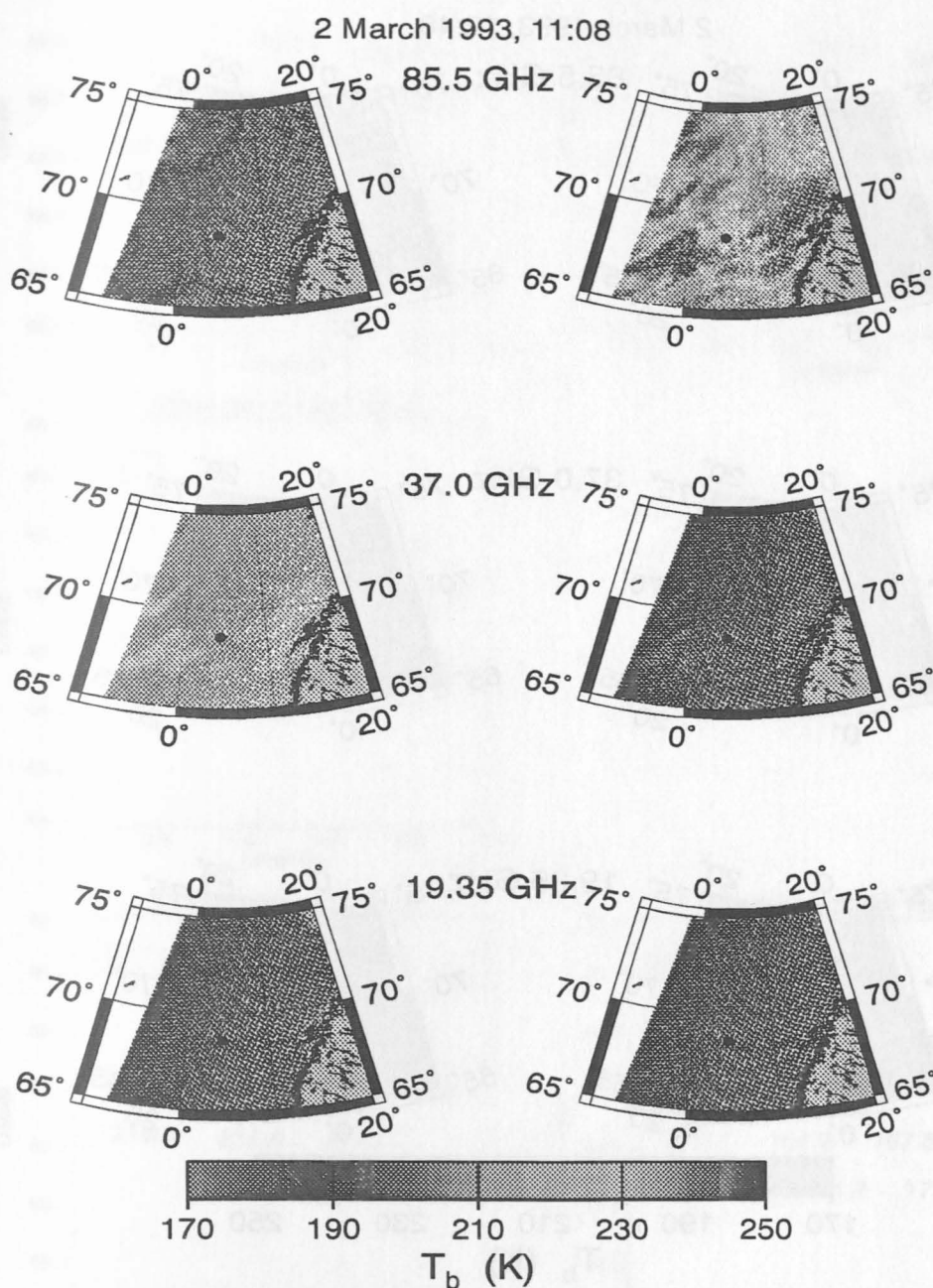


Figure 42 SSM/I brightness temperature distributions around the Polarstern on 2 March 93, 11:08 UT (case 1); the ship's position is indicated by the black bullet.

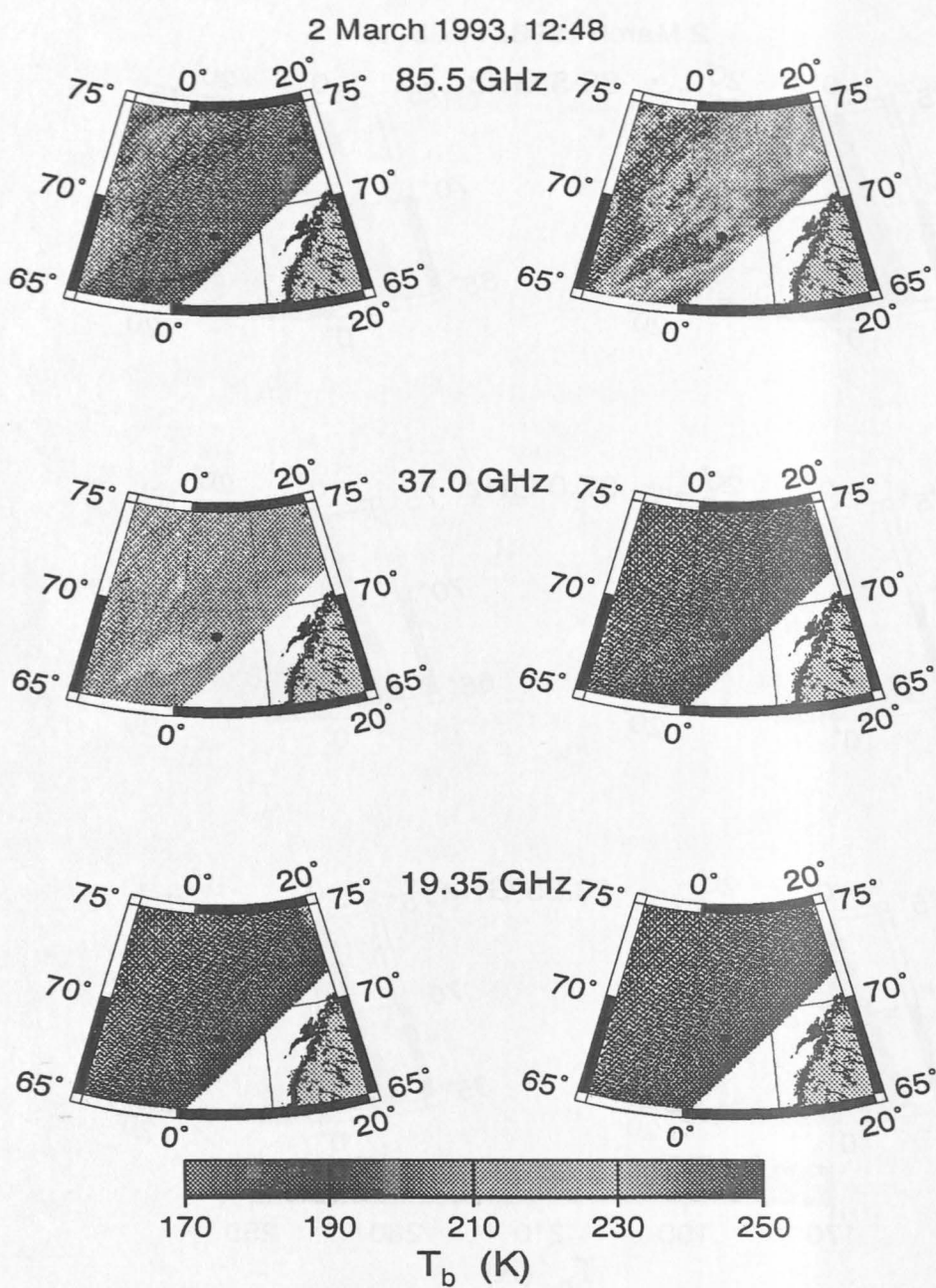


Figure 43 SSM/I brightness temperature distributions around the Polarstern on 2 March 93, 12:48 UT (case 1); the ship's position is indicated by the black bullet.

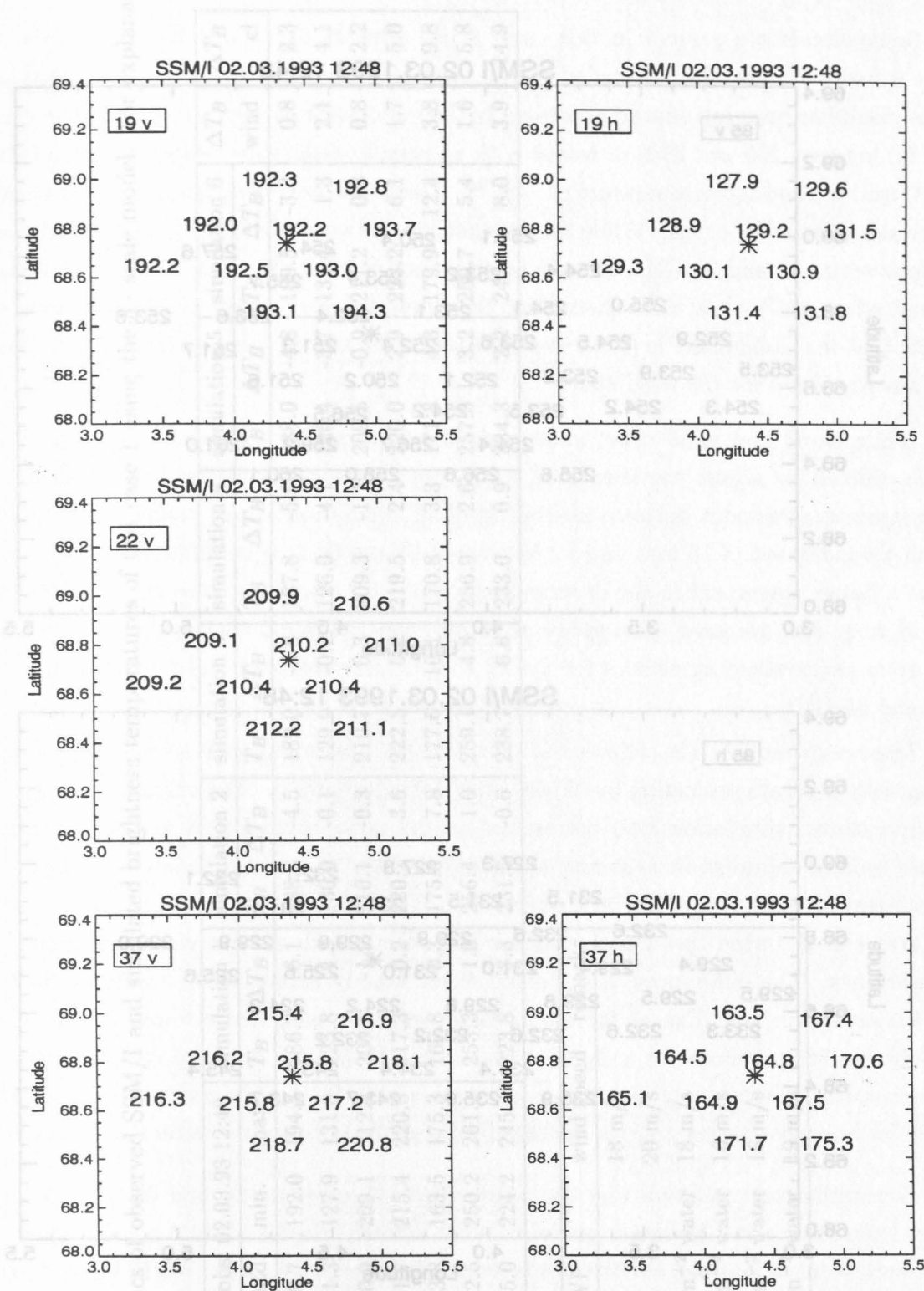


Figure 44 Observed SSM/I brightness temperatures of the 10 pixels nearest to the ship position (\*) for case 1 (2 March 1993 12:48 UT).



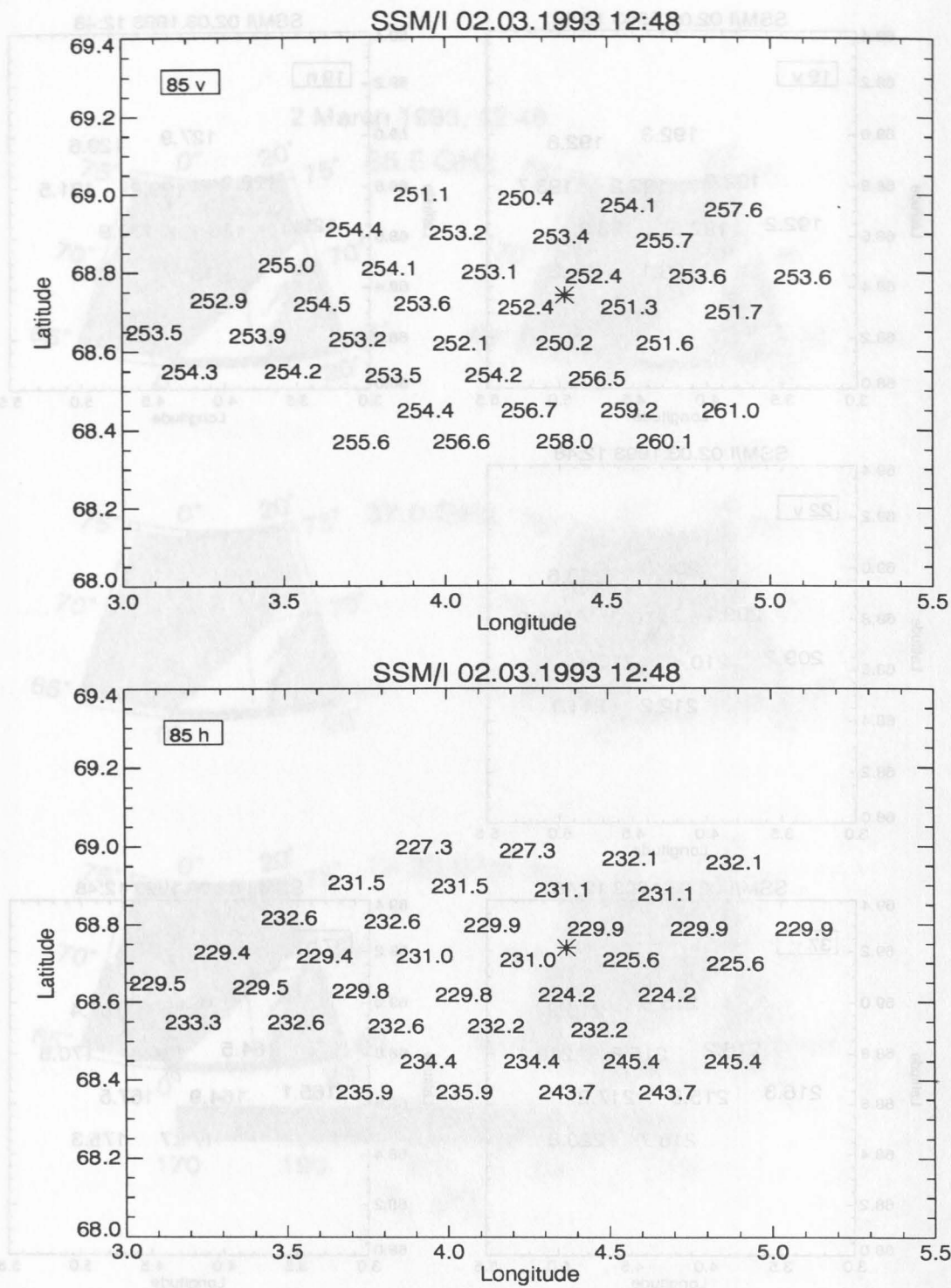


Figure 45 Observed SSM/I brightness temperatures of the 85 GHz channels nearest to ship position (\*) for case 1 (2 March 1993 12:48 UT).

Table 9 Statistics of observed SSM/I and simulated brightness temperatures of test case 1 using the 3- scale model. For explanation see text.

SSM/I F10 $T_B$ obs. 02.03.93 12:48					simulation 1		simulation 2		simulation 3		simulation 4		simulation 5		simulation 6		$\Delta T_B$	$\Delta T_B$
chan.	mean	std.	min.	max.	$T_B$	$\Delta T_B$	$T_B$	$\Delta T_B$	$T_B$	$\Delta T_B$	$T_B$	$\Delta T_B$	$T_B$	$\Delta T_B$	$T_B$	$\Delta T_B$	wind	cl
19 v	192.8	0.7	192.0	194.3	186.7	-6.1	188.3	-4.5	189.0	-3.8	187.8	-5.0	188.0	-4.8	189.5	-3.3	0.8	2.3
19 h	130.1	1.3	127.9	131.8	125.8	4.3	130.0	-0.1	129.9	-0.2	126.0	-4.1	126.4	-3.7	131.4	1.3	2.1	4.1
22 v	210.4	0.9	209.1	212.2	208.5	-1.9	210.1	-0.3	210.7	0.3	209.3	-1.1	209.5	-0.9	211.2	0.8	0.8	2.2
37 v	217.1	1.7	215.4	220.8	217.3	0.2	220.7	3.6	222.3	5.2	219.5	2.4	220.0	2.9	223.2	6.1	1.7	5.0
37 h	167.5	3.8	163.5	175.3	167.8	0.3	175.3	7.8	177.6	10.1	170.8	3.3	171.8	4.3	179.9	12.4	3.8	9.8
85 v	254.3	2.5	250.2	261.1	253.3	-1.0	256.4	1.0	259.1	4.8	256.9	2.6	257.5	3.2	259.7	5.4	1.6	5.8
85 h	232.1	5.0	224.2	245.4	223.8	-8.3	231.5	-0.6	238.7	6.6	233.0	0.9	234.3	2.2	240.1	8.0	3.9	14.9

Sim.	cloud LWP	wind speed	remarks
1	none	18 m/s	
2	none	20 m/s	
3	0.10 kg m <sup>-2</sup> water	18 m/s	
4	0.10 kg m <sup>-2</sup> water	16 m/s	
5	0.11 kg m <sup>-2</sup> water	16 m/s	
6	0.09 kg m <sup>-2</sup> water	19 m/s	

function within a  $\pm 2$  m/s range.

Since clouds are present in this case, a low altitude cloud with a liquid water path  $l = 0.1 \text{ kg m}^{-2}$  has been modelled with a surface wind speed of 18 m/s (simulation 3). The cloud has been introduced according to the radiosonde data (relative humidity greater 95 %) between 200 and 2000 m height with an equally distributed water content of  $0.05 \text{ g kg}^{-1}$  and a cloud top temperature of  $-4.6^\circ\text{C}$ . The brightness temperatures of all channels increase due to the cloud. While the comparison between observation and simulation is improved for 19 and 22 GHz, there is deterioration for the other channels. The estimated cloud effect ( $\Delta T_{B,cl}$ ) is more than twice the simulated wind effect and of the same sign. Note that the cloud effect is particularly strong for 37 and 85 GHz horizontal polarization as already found for the wind effect.

While cloud and wind effect show very similar changes in brightness temperatures, it is difficult to adjust the simulated wind speed and/or cloud liquid water to find an appropriate agreement between observation and simulation for all channels. Simulation with a wind speed of 16 m/s and a  $l$  between  $0.10$  and  $0.11 \text{ kg m}^{-2}$  (simulations 4 and 5) give a better agreement to the observed brightness temperatures than with a wind speed of 18 m/s. An increased wind speed of 19 m/s and reduced  $l = 0.090 \text{ kg m}^{-2}$  (simulation 6) gives an excellent agreement for the 19 and 22 GHz channels, but large deviations for 37 and 85 GHz.

The ocean module also allows the simulation of the ocean surface reflection / emission with a parameterization by Wisler and Hollinger (1977). The calculated brightness temperatures (simulation 7–9) correspond to the same environment as used for the 3-scale module (simulation 1–3) and are given in Tab. 10. The estimated wind effect is much smaller than that of the 3-scale module. Therefore this formulation is less sensitive to errors of the wind speed observation. The effects of clouds are very similar for both approaches. The differences in the cloud effect mainly result from emission differences of the ocean surface. Except for the 19 GHz vertically polarized channel, the simulated brightness temperatures for a cloudy atmosphere (simulation 9) agree very well with the observations. Unfortunately there are no restored SSM/I brightness temperatures available for both overpasses and the effects of different footprint sizes cannot be analyzed.

To summarize it is found that the results of the 3-scale model and the parameterization from Wisler and Hollinger give somewhat different results. While a good agreement between observations and simulations is found with  $U = 18 \text{ m/s}$  and  $l = 0.10 \text{ kg m}^{-2}$  for the Wisler and Hollinger formulation, the 3-scale model gives closest simulations for  $U = 16 \text{ m/s}$  and  $l = 0.11 \text{ kg m}^{-2}$ . However, keeping in mind a highly variable cloudiness and a possible correlation of clouds with local wind speed anomalies, it is not possible to draw any conclusion which surface model fits better to the observed brightness temperatures. The influence of other parameter errors, such as salinity or sea surface temperature have also



Table 10 Statistics of observed SSM/I and simulated brightness temperatures of test case 1 using the parameterization of Wisler and Hollinger (1977)

SSM/I F10 $T_B$ obs. 02.03.93 12:48					simulation 7		simulation 8		simulation 9		$\Delta T_{B,wind}$	$\Delta T_{B,cloud}$
chan.	mean	std.	min.	max.	$T_B$	$\Delta T_B$	$T_B$	$\Delta T_B$	$T_B$	$\Delta T_B$		
19 v	192.8	0.7	192.0	194.3	185.6	-7.2	186.2	-6.6	187.8	-5.0	0.3	2.2
19 h	130.1	1.3	127.9	131.8	126.8	-3.3	129.4	-0.7	130.6	-0.5	1.2	3.7
22 v	210.4	0.9	209.1	212.2	206.1	-4.3	206.6	-3.8	208.3	2.1	0.2	2.2
37 v	217.1	1.7	215.4	220.8	211.6	-5.5	212.3	-4.8	216.8	-0.3	0.3	5.2
37 h	167.5	3.8	163.5	175.3	158.2	-9.3	161.0	-6.5	167.7	0.2	1.4	9.5
85 v	254.3	2.5	250.2	261.1	248.5	-5.8	248.9	-5.4	255.5	1.2	0.2	7.0
85 h	232.1	5.0	224.2	245.4	211.0	-21.1	212.8	-19.3	228.4	-3.7	1.3	17.4

Sim.	cloud	wind speed	remarks
7	none	18 m/s	
8	none	20 m/s	
9	0.1 kg m <sup>-2</sup> water	18 m/s	

been modeled. But changes of these parameters within expected ranges caused changes in brightness temperatures only in the order of a few tenth of a Kelvin. The main contributions to the radiative signature arises from the wind speed (surface roughness) and clouds. However, to perform a higher quality validation for the ocean module, a cloud-free situation is required, to exclude uncertainties caused by the presence of clouds.

## 4.4 Case 2: Ice, small cloud fraction, winter

### 4.4.1 Synoptic Situation

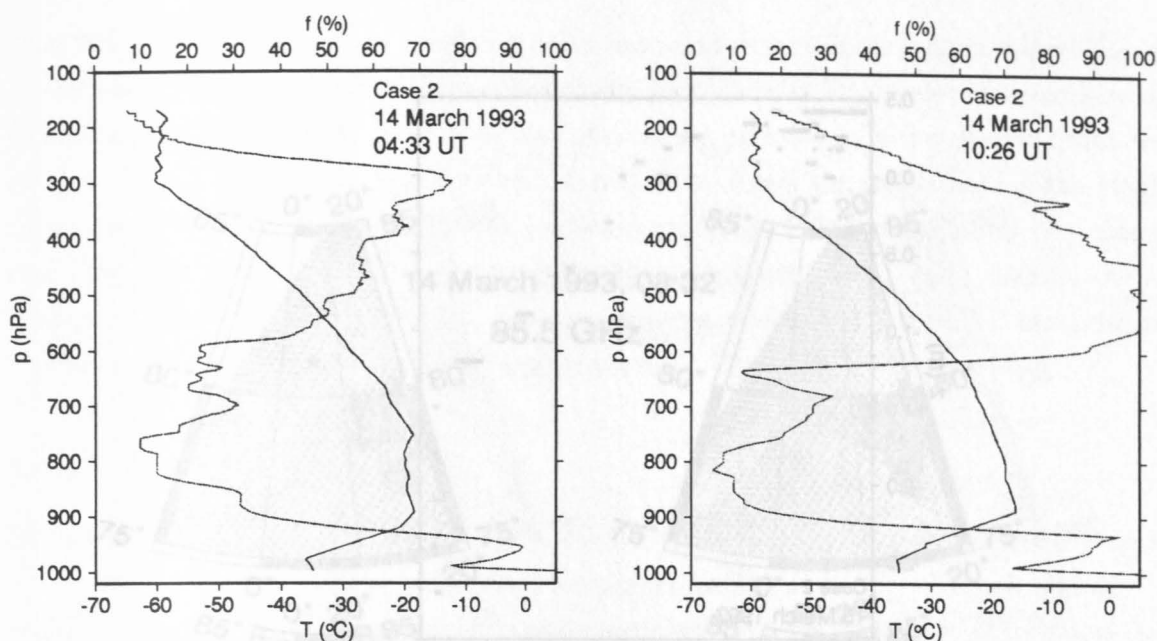
Unlike the first case this situation describes the arctic atmosphere over the ice-covered ocean. It spans the time period from 0 to 10 UT on 14 March 1993 where a cyclone family with a leading low over Svalbard and the following one in the southern Greenland Sea determines the meteorological situation at the ice-floe station, located near  $5.4^{\circ}\text{E}$ ,  $81.1^{\circ}\text{N}$ . Before 6 UT snow grains (Schneegriesel) were falling. However, at satellite overpass times no significant weather was observed. Between 4 and 5 UT stratocumulus stratiformis was formed with a cloud base between 600 and 1000 m. After 9 UT one to two octas cirrus or cirrostratus have been observed while later, near 11 UT, more than half of the sky was covered by clouds at middle tropospheric levels. The visibility was between 2 and 10 km due to humid haze following the snow fall in the early morning. The wind at the ice-floe station comes from northwesterly directions during this day. Hence, the co-located SSM/I measurements should be widely unaffected by the atmospheric liquid or ice water content. The surface air temperature varied between  $-36.2$  and  $-32.2$   $^{\circ}\text{C}$  during the time period under consideration. The water temperature as measured from the R/V Polarstern was constant at  $-1.6$   $^{\circ}\text{C}$ . Table 11 summarizes the synoptic data used for the simulations of the brightness temperatures.

Table 11 Synoptic observations for case 2.

date : 14.3.1993	position : $5.4^{\circ}\text{E}$ / $81.1^{\circ}\text{N}$	
SSM/I overpass : 08:32 UT	radiosonde launch : 04:33 UT	synop : 09:00 UT
pressure : 999.2 hPa	$T_a$ : $-36.0$ $^{\circ}\text{C}$	humidity : 74 %
wind speed : 8.2 m/s	$T_0$ : $-1.6$ $^{\circ}\text{C}$	cloud : 10005
wind dir. : $293^{\circ}$	PWC : $1.3\text{ kg m}^{-2}$	$\Delta T_{ice-snow}$ : $-12.8\text{ K}$

### 4.4.2 Atmospheric Parameters

Radiosondes have been launched at 04:33 and 10:26 UT (Fig. 46) indicating a strong temperature inversion below 900 hPa with a moisture content reaching peak values of the relative humidity between 90 and 100%. A second layer with enhanced moisture is seen between 600 and 300 hPa. This layer starts with humidities well below 80% as shown



**Figure 46** Temperature (contiguous) and relative humidity (dotted) profiles for case 2; given times are launch times.

by the first radiosonde ascent while the later humidity profile indicates saturation in the layer between 650 and 550 hPa, well fitting the observation of increased cloud amount in the late morning. The temperature profiles as measured by the two sondes are similar; maximum deviations up to 3 K occur above the top of the inversion layer.

#### 4.4.3 Surface Parameters

The thermometer chain was deployed into the ice during the days before 14 March so that the measurements which began on this day are still subject to the temperature disturbance caused by the ice drills necessary to lower the thermometer chain. Therefore, the ice temperatures measured one day later are assumed to be more representative for the ice profiles (Figure 47). The snow cover was about 40 cm (depth  $z=0.0$  m indicates the snow-ice interface). The ice-water horizon was at -1.5 m. As seen in the figure there is still a great variation of temperatures in the snow. Those clustering at higher temperatures are assumed to represent the real values. The ice temperatures vary between -12 and -4 °C on this day. The snow temperatures are far lower, triggered by the low air temperature they show values down to -30 °C.

Six snow cores have been taken in the time period between 11 and 19 May 1993 in order to analyse snow density and crystal structure. The cores reveal two different snow layers, an upper layer of fine-grained low-density snow and a lower layer of coarse-grained high-density snow. The layers were separated at a level of  $18 \pm 2$  cm above the ice horizon. The sea-ice parameters used for the simulations are given in Tab. 12. Because the temperatures

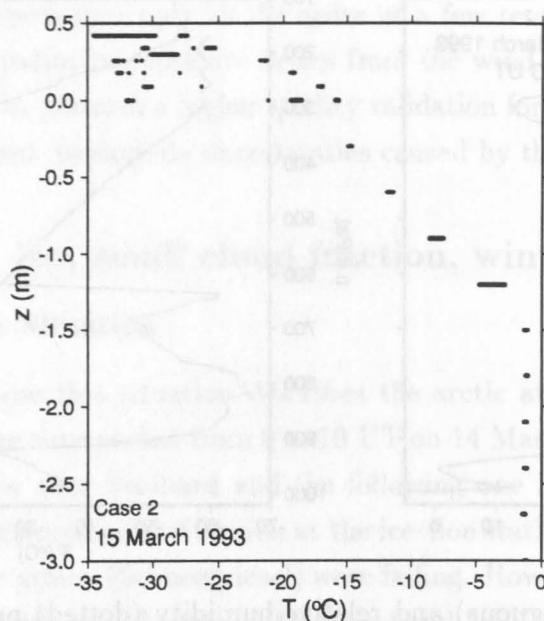


Figure 47 Variation of snow, ice and water temperatures during 24 hours covering case 2.

Table 12 Input parameter for sea ice module for case 2. For explanation of parameters see Tab. 6

$z$	$T_i$	$\rho$	$D_{GS}$	$l_f$	$D_{GI}$	$D_B$	$S$	$\theta_B$	$B_R$	#	
-9.999	272.0	1.000	0.00	1.000	0.00	0.0	32.0	0.0	0.000E+00	1	water
-1.590	272.0	0.892	0.00	0.000	10.00	1.2	2.3	24.0	0.250E-04	2	ice
-1.290	269.3	0.883	0.00	0.000	10.00	1.2	2.1	24.0	0.250E-04	3	
-0.990	265.0	0.872	0.00	0.000	10.00	1.2	1.4	24.0	0.250E-04	4	
-0.690	261.5	0.853	0.00	0.000	10.00	1.2	0.7	24.0	0.250E-04	5	
-0.390	258.4	0.814	0.00	0.000	10.00	1.2	0.2	24.0	0.250E-04	6	
-0.090	254.3	0.728	2.00	0.000	0.00	3.0	0.0	54.7	0.100E+01	7	snow
-0.060	243.9	0.460	2.00	0.000	0.00	5.0	0.0	54.7	0.100E+01	8	
-0.030	241.5	0.100	0.75	0.000	0.00	1.2	0.0	0.0	0.100E+01	9	
0.000	241.5	0.100	0.75	0.000	0.00	1.2	0.0	0.0	0.100E+01	10	

are far below the freezing point, no liquid water fraction was assumed for the snow layer. The fresh snow is represented by a relatively small density of  $0.1 \text{ g/cm}^3$  in the upper snow layer.

#### 4.4.4 SSM/I Observations

SSM/I scenes including the ice-floe station have been recorded at 08:32 and 10:12 UT. AVHRR imagery supplied by NOAA-10 at 08:29 UT clearly shows an ice coverage greater

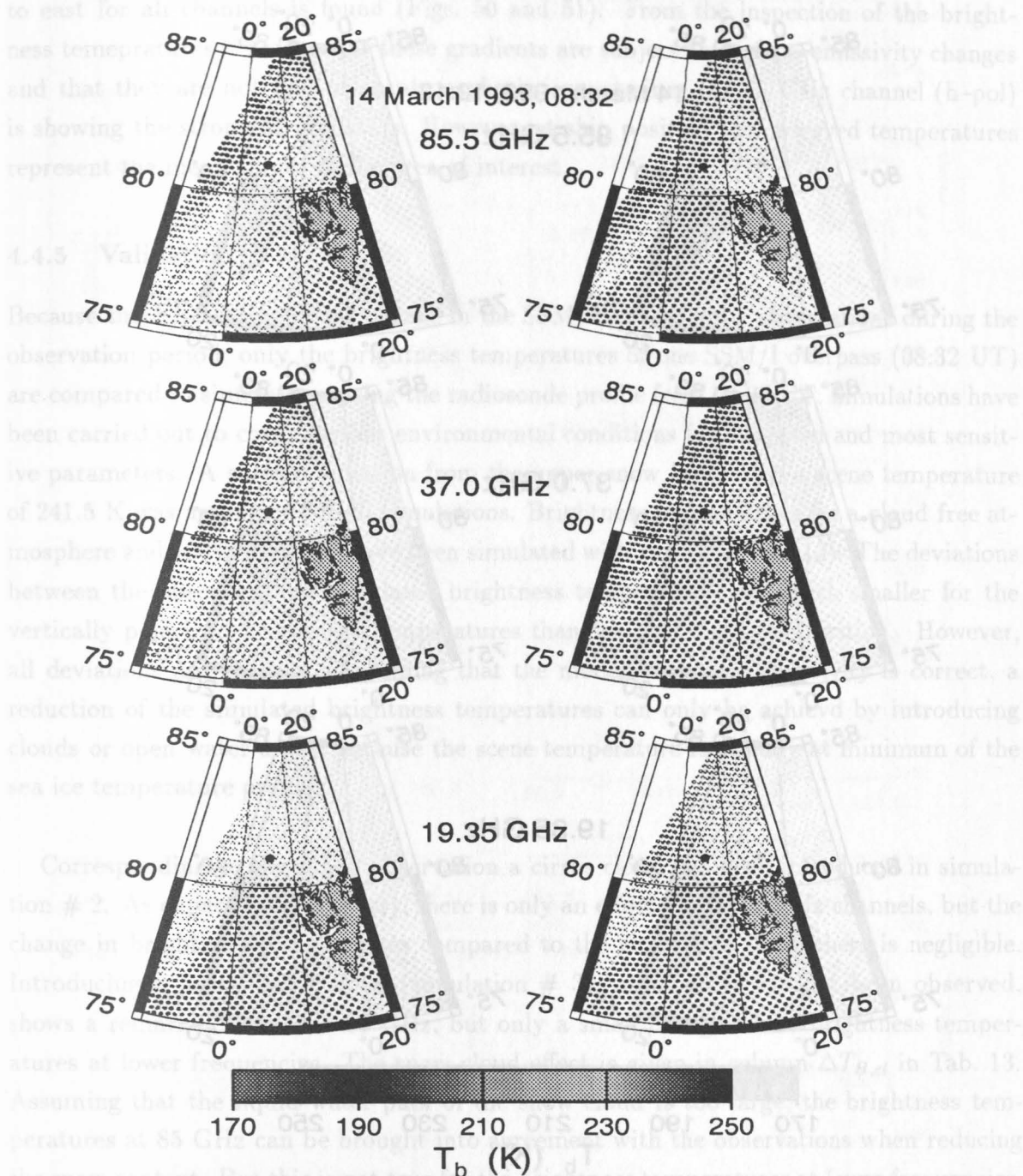


Figure 48 SSM/I brightness temperature distributions around the ice-floe station on 14 March 93, 08:32 UT; the station is indicated by the black bullet.



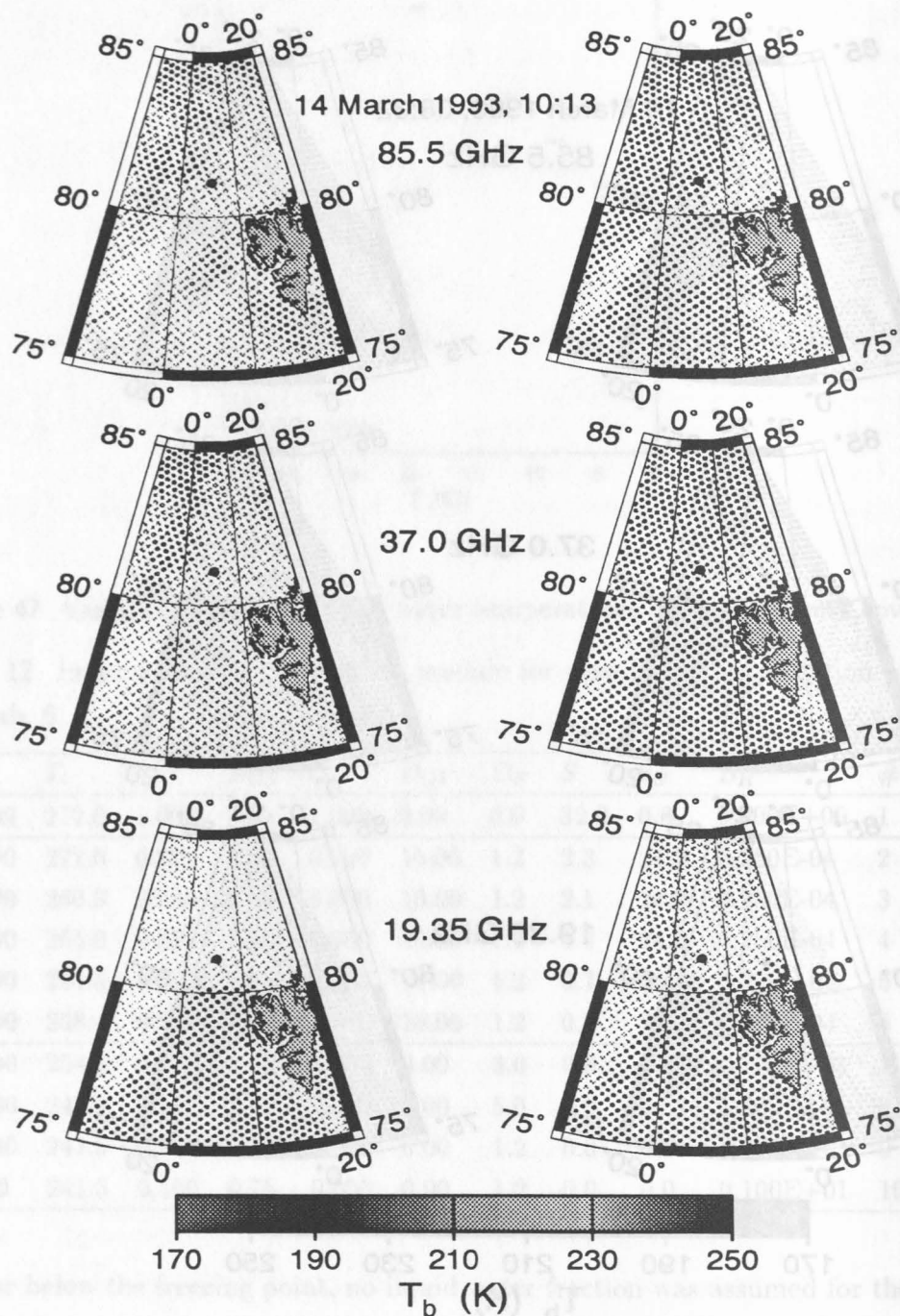


Figure 49 SSM/I brightness temperature distributions around the ice-floe station on 14 March 93, 10:13 UT; the station is indicated by the black bullet.

than 90%. Several leads are identified with temperatures indicating open water. Images of the two SSM/I overpasses (Figs. 48 and 49) show similar brightness-temperature distributions. In the vicinity of the ice-floe station an increase of a few Kelvin from west to east for all channels is found (Figs. 50 and 51). From the inspection of the brightness temperatures it seems that these gradients are subject to surface-emissivity changes and that they are not due to an atmospheric impact since the 19 GHz channel (h-pol) is showing the strongest gradients. However, at ship position the observed temperatures represent the mean values of the area of interest.

#### 4.4.5 Validation

Because there is no significant change in the SSM/I and synoptic observations during the observation period, only the brightness temperatures of one SSM/I overpass (08:32 UT) are compared to simulations using the radiosonde profile from 04:33 UT. Simulations have been carried out to cover various environmental conditions for unknown and most sensitive parameters. A surface emission from the upper snow layer with a scene temperature of 241.5 K was assumed for all simulations. Brightness temperatures for a cloud free atmosphere and 100% ice cover have been simulated with run # 1 (Tab. 13). The deviations between the observed and simulated brightness temperatures are much smaller for the vertically polarized brightness temperatures than for horizontal polarization. However, all deviations are positive. Assuming that the modelled sea ice emissivity is correct, a reduction of the simulated brightness temperatures can only be achieved by introducing clouds or open water areas, because the scene temperature is already at minimum of the sea ice temperature profile.

Corresponding to the synop observation a cirrus cloud has been introduced in simulation # 2. As expected from theory, there is only an effect on the 85 GHz channels, but the change in brightness temperatures compared to the cloud free atmosphere is negligible. Introducing a heavy snow cloud (simulation # 3), although it has not been observed, shows a remarkable effect on 85 GHz, but only a small change of the brightness temperatures at lower frequencies. The snow cloud effect is given in column  $\Delta T_{B,cl}$  in Tab. 13. Assuming that the liquid water path of the snow cloud is too large, the brightness temperatures at 85 GHz can be brought into agreement with the observations when reducing the snow content. But this is not true for the brightness temperatures at lower frequencies.

The ice coverage estimated by the NASA sea ice algorithm (Cavalieri, 1992) from the observed brightness temperatures is about 90% (50% first year and 40% multi year ice) for all SSM/I pixels, which is in agreement with the AVHRR image. Simulation # 4 computed the brightness temperatures for this ice coverage. Except for the 37 GHz channels the agreement with observations is very good. The open water effect (the change of the



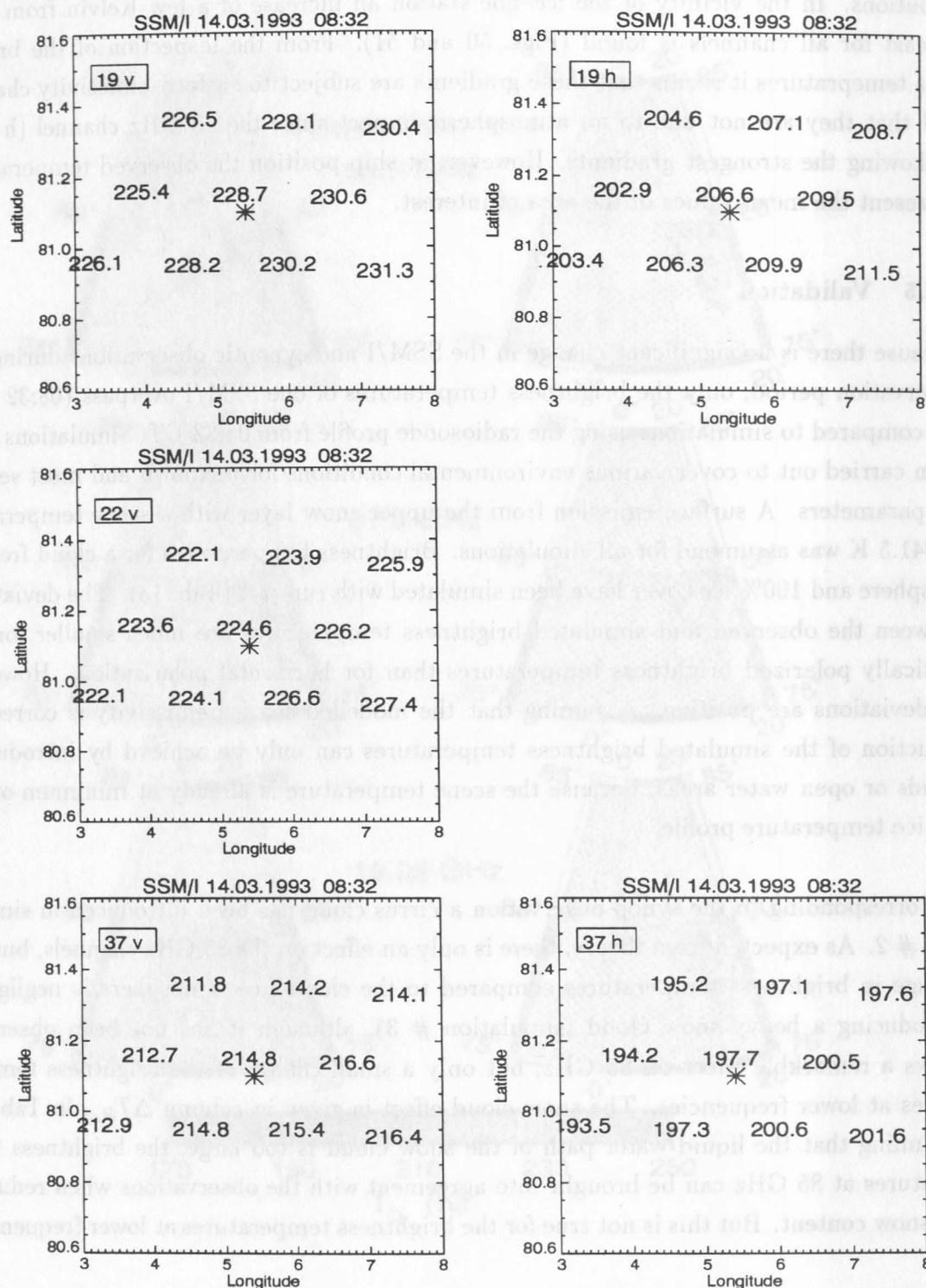


Figure 50 Observed SSM/I brightness temperatures (lower frequency channels) of the 10 nearest pixels to ice-floe station (\*) for 14 March 1993 (case 2).

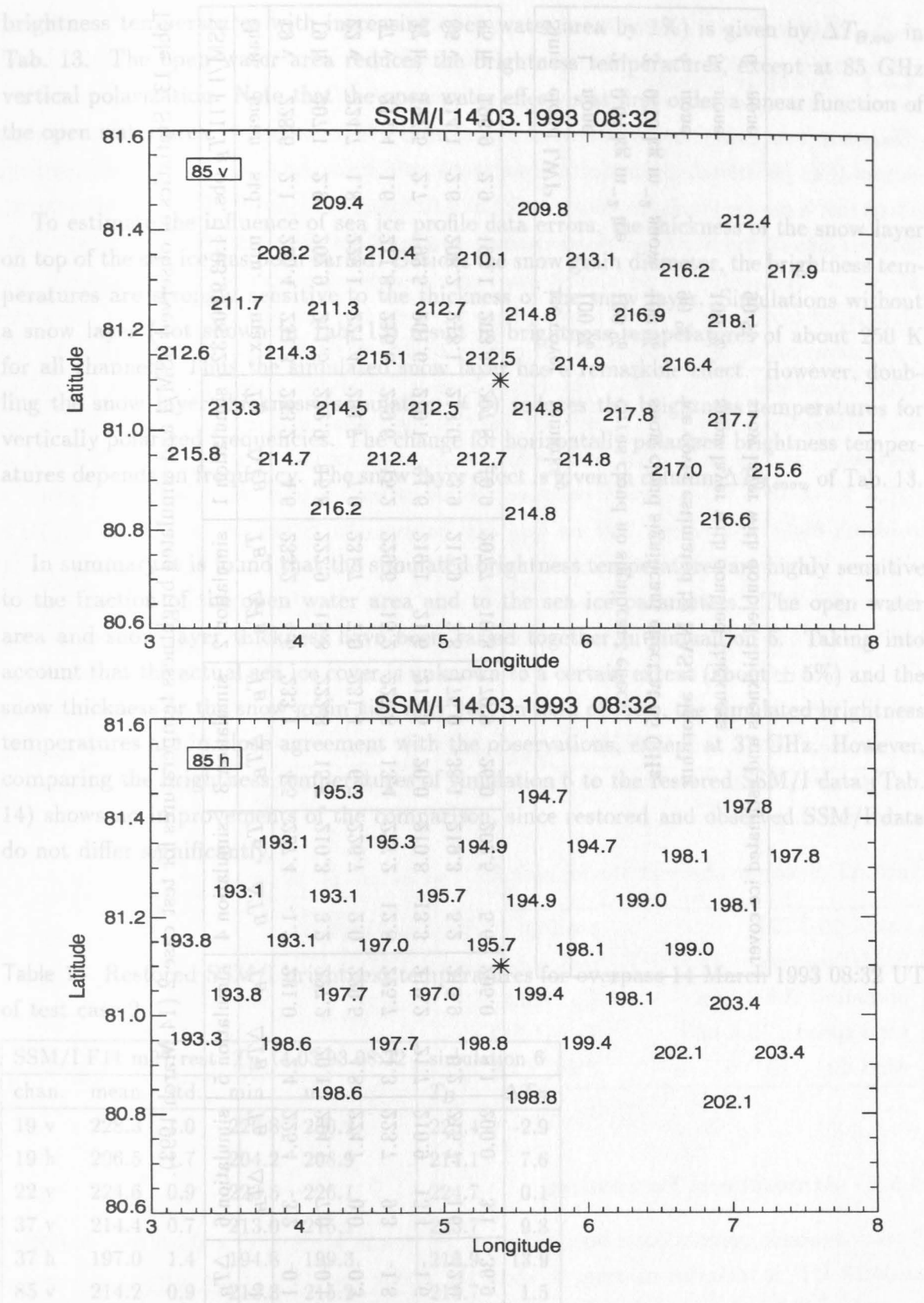


Figure 51 Observed SSM/I brightness temperatures of the 85 GHz channels nearest to ice-floe station (\*) for 14 March 1993 (case 2).

Table 13 Statistics of observed SSM/I and simulated brightness temperatures for test case 2 (14 March 1993).

SSM/I F11 $T_B$ obs. 14.03.93 08:32					simulation 1		simulation 2		simulation 3		simulation 4		simulation 5		simulation 6		$\Delta T_B$	$\Delta T_B$	$\Delta T_B$
chan.	mean	std.	min.	max.	$T_B$	$\Delta T_B$	$T_B$	$\Delta T_B$	$T_B$	$\Delta T_B$	$T_B$	$\Delta T_B$	$T_B$	$\Delta T_B$	$T_B$	$\Delta T_B$	cl	ow	snow
19 v	228.6	2.1	225.4	231.3	233.2	4.6	233.2	4.6	233.1	4.5	227.4	-1.2	231.0	2.4	225.4	-3.2	-0.1	-0.6	-2.2
19 h	207.1	2.9	202.9	211.5	222.9	15.8	222.9	15.8	222.8	15.7	210.3	3.2	227.2	20.1	214.1	7.0	-0.1	-1.3	4.3
22 v	224.7	1.8	222.1	227.4	231.7	7.0	231.7	7.0	231.4	6.7	226.7	2.0	229.5	4.8	224.7	0.0	-0.3	-0.5	-2.2
37 v	214.4	1.6	211.8	216.6	229.6	15.2	229.6	15.2	227.8	13.4	227.2	12.8	225.7	11.3	223.7	9.3	-1.8	-0.2	-3.9
37 h	197.5	2.7	193.5	201.6	219.1	21.6	219.1	21.6	217.5	20.0	210.8	13.3	219.2	21.7	210.9	13.4	-1.6	-0.8	0.1
85 v	214.1	2.6	208.2	218.1	218.0	3.9	217.9	3.8	176.0	-38.1	219.3	5.2	213.9	-0.2	215.7	1.6	-42.0	0.1	-4.1
85 h	196.9	2.9	193.1	203.4	207.8	10.9	207.7	10.8	170.9	-26.0	202.5	5.6	205.0	8.1	200.0	3.1	-36.9	-0.5	-2.8

Sim.	cloud LWP	ice cover	remarks
1	none	100 %	
2	0.04 kg m <sup>-2</sup> ice	100 %	cirrus cloud no significant effect
3	0.10 kg m <sup>-2</sup> snow	100 %	snow cloud significant effect at 85 GHz
4	none	90 %	ice cover estimated by NASA algorithm
5	none	100 %	snow layer with doubled thickness
6	none	90 %	snow layer with doubled thickness and estimated ice cover

brightness temperatures with increasing open water area by 1%) is given by  $\Delta T_{B,ow}$  in Tab. 13. The open water area reduces the brightness temperatures, except at 85 GHz vertical polarization. Note that the open water effect is at first order a linear function of the open water area.

To estimate the influence of sea ice profile data errors, the thickness of the snow layer on top of the sea ice has been varied. Besides the snow grain diameter, the brightness temperatures are strongly sensitive to the thickness of the snow layer. Simulations without a snow layer (not shown in Tab. 13) result in brightness temperatures of about 250 K for all channels. Thus the simulated snow layer has a remarkable effect. However, doubling the snow layer thickness (simulation # 5) reduces the brightness temperatures for vertically polarized frequencies. The change for horizontally polarized brightness temperatures depends on frequency. The snow layer effect is given in column  $\Delta T_{B,snow}$  of Tab. 13.

In summary it is found that the simulated brightness temperatures are highly sensitive to the fraction of the open water area and to the sea ice parameters. The open water area and snow layer thickness have been varied together in simulation 6. Taking into account that the actual sea ice cover is unknown to a certain extent (about  $\pm 5\%$ ) and the snow thickness or the snow grain size may vary in field of view, the simulated brightness temperatures are in close agreement with the observations, except at 37 GHz. However, comparing the brightness temperatures of simulation 6 to the restored SSM/I data (Tab. 14) shows no improvements of the comparison, since restored and observed SSM/I data do not differ significantly.

**Table 14** Restored SSM/I brightness temperatures for overpass 14 March 1993 08:32 UT of test case 2.

SSM/I F11 m37 rest. $T_B$ 14.03.93 08:32					simulation 6	
chan.	mean	std.	min.	max.	$T_B$	$\Delta T_B$
19 v	228.3	1.0	226.8	230.2	225.4	-2.9
19 h	206.5	1.7	204.2	208.9	214.1	7.6
22 v	224.6	0.9	223.5	226.1	224.7	0.1
37 v	214.4	0.7	213.0	215.1	223.7	9.3
37 h	197.0	1.4	194.8	199.3	210.9	13.9
85 v	214.2	0.9	212.3	215.2	215.7	1.5
85 h	197.7	1.2	195.7	199.4	200.0	2.3



## 4.5 Case 3: Ice, overcast sky, winter

### 4.5.1 Synoptic Situation

This case lasts from 8 to 16 UT on 16 March 1993 where the ice-floe station was drifting near 5.0°E, 80.9°N. A warm front, connected to a low over Bear Island, extends from about 85°N to the northern Greenland Sea and separates warm air advected from the Barents Sea to the northwest from cold air coming from the north. The situation at the station is represented by an almost overcast sky showing stratocumulus stratiformis and stratus nebulosus clouds with a cloud base between 100 and 300 m. At 9 UT the cloud cover temporarily decreased to 4 octas only. Between 10 and 11 UT and after 14 UT single snow stars were falling from those clouds, otherwise humid haze was prevailing with visibilities below 5 km. The wind was blowing from northerly directions with speeds between 7 and 10 m/s. The surface air temperature varied from -26.6 °C at 8 UT to -25.5 °C at 16 UT. The water temperature below the ice pack was close to -1.5 °C. A research flight was carried out on this day between 09:28 and 11:40 UT by the DLR Falcon. The aircraft did not reach the ice floe but did ice and atmosphere observations 90 km southeast of the station, close to the ice edge. The cloud situation during the flight is the same as observed at the ice floe, namely, seven to eight octas stratus and stratocumulus. The areal ice concentration observed is between 80 and 90%. On another research flight, one day later between 09:35 and 12:19 UT the aircraft passed the Polarstern observing an ice cover of 100%. An AVHRR image at 09:21 UT shows warm stratiform clouds being too opaque for any view down to the surface. The synoptic data used for the validation is given in Table 15.

Table 15 Synoptic observations for case 3.

date : 16.3.1993	position : 4.98° E / 80.89° N	
SSM/I overpass : 08:07 UT	radiosonde launch : 04:18 UT	synop : 08 UT
pressure : 986.2 hPa	$T_a$ : -26.6 °C	humidity : 80 %
wind speed : 10.4 m/s	$T_0$ : -1.5 °C	cloud : 77-7-
wind dir. : 13 °	PWC : 4.8 kg m <sup>-2</sup>	$\Delta T_{ice-snow}$ : -7.8 K

### 4.5.2 Atmospheric Parameters

Two radiosonde ascents have been taken at 10:29 and 16:28 UT; a third one, launched at 04:18 UT, is included in order to show the strong variation of the atmospheric water vapour profile during this day (Fig. 52). While the first radiosonde shows high moisture with relative humidities greater than 90% for the entire lower 5 km of the atmosphere several layers are dried as seen in the subsequent humidity profiles. The second radiosonde shows layers with lower water-vapour amounts close to the surface, near 720, 580, and

230 hPa. In the profile observed at 16:28 UT one can see that the moisture in the lowest level increased again while two very dry layers established close to 800 and 480 hPa with relative humidities less than 20%. Another dry layer is seen at 600 hPa with a minimum of less than 40%. In the same time period the temperature profile is modified also, but mainly below 800 hPa. Two inversions can be identified in the profiles, the strong near-surface inversion and a second one just below 850 hPa. The latter weakened between 4 and 11 UT and strengthened again in the following time period as seen in the ascent starting at 16:28

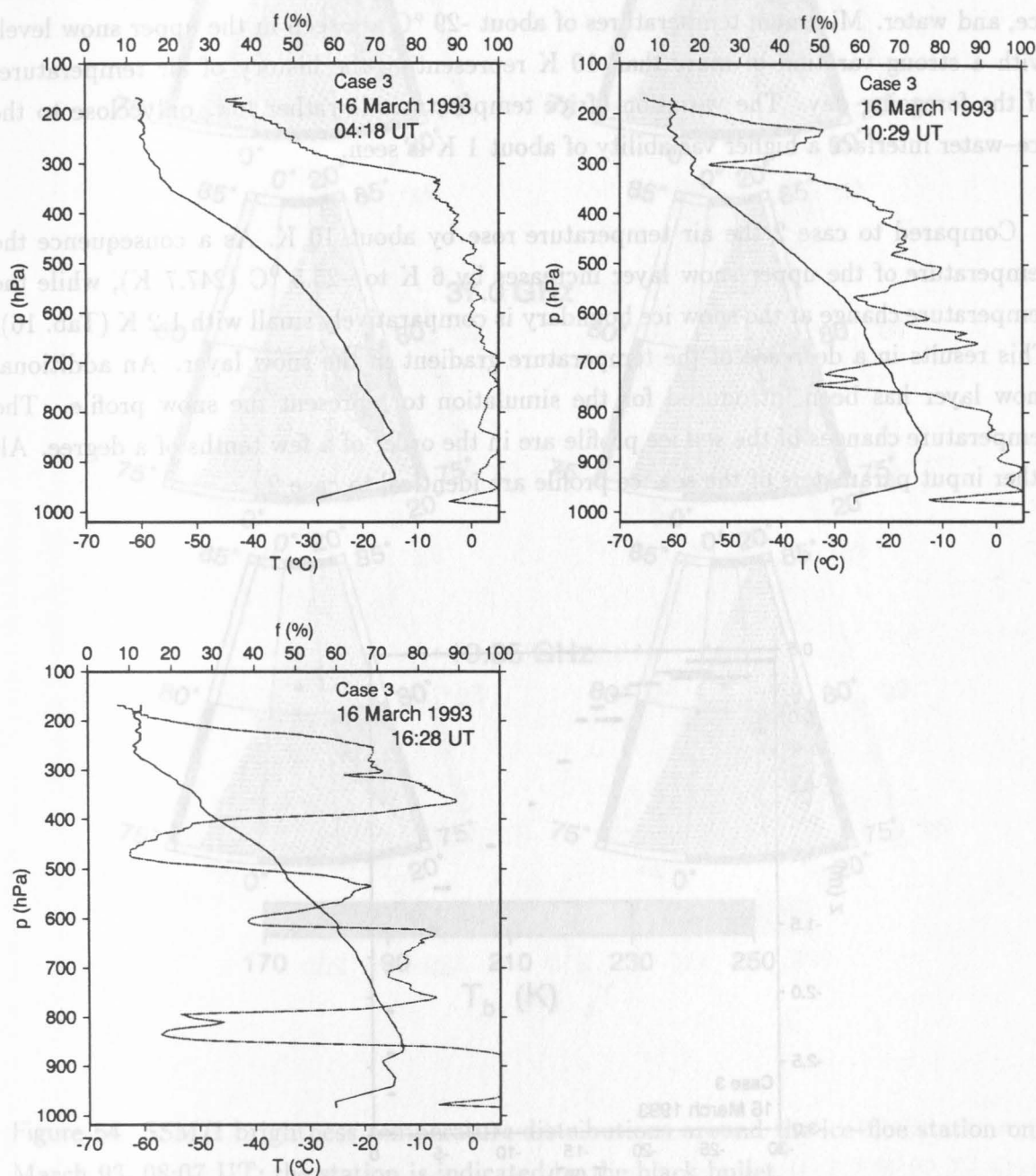


**Figure 52** Temperature (contiguous) and relative humidity (dotted) profiles for case 3; given times are launch times.

UT. Concurrently, this inversion layer sinks from 850 to 870 hPa indicating subsiding air masses due to the increasing impact of an anticyclone centered over the north pole. The absolute differences between the temperature profiles are up to 5 K in the inversion layers observed.

#### 4.5.3 Surface Parameters

The snow and ice profiles for this situation (Figure 53) show a clear separation of snow, ice, and water. Minimum temperatures of about  $-29^{\circ}\text{C}$  are seen in the upper snow levels with a strong variation of more than 10 K representing the history of air temperatures of the foregoing day. The variation of ice temperatures is rather low, only close to the ice-water interface a higher variability of about 1 K is seen.

Compared to case 2 the air temperature rose by about 10 K. As a consequence the temperature of the upper snow layer increases by 6 K to  $-25.5^{\circ}\text{C}$  (247.7 K), while the temperature change at the snow ice boundary is comparatively small with 1.2 K (Tab. 16). This results in a decrease of the temperature gradient in the snow layer. An additional snow layer has been introduced for the simulation to represent the snow profile. The temperature changes of the sea ice profile are in the order of a few tenths of a degree. All other input parameters of the sea ice profile are identical to case 2.

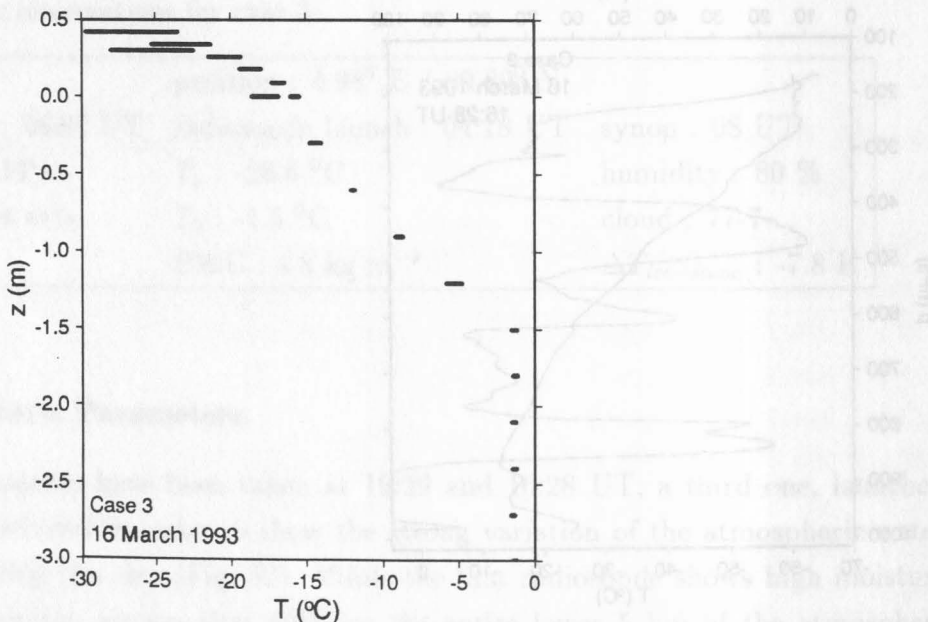


Figure 53 Variation of snow, ice and water temperatures during 24 hours covering case 3.



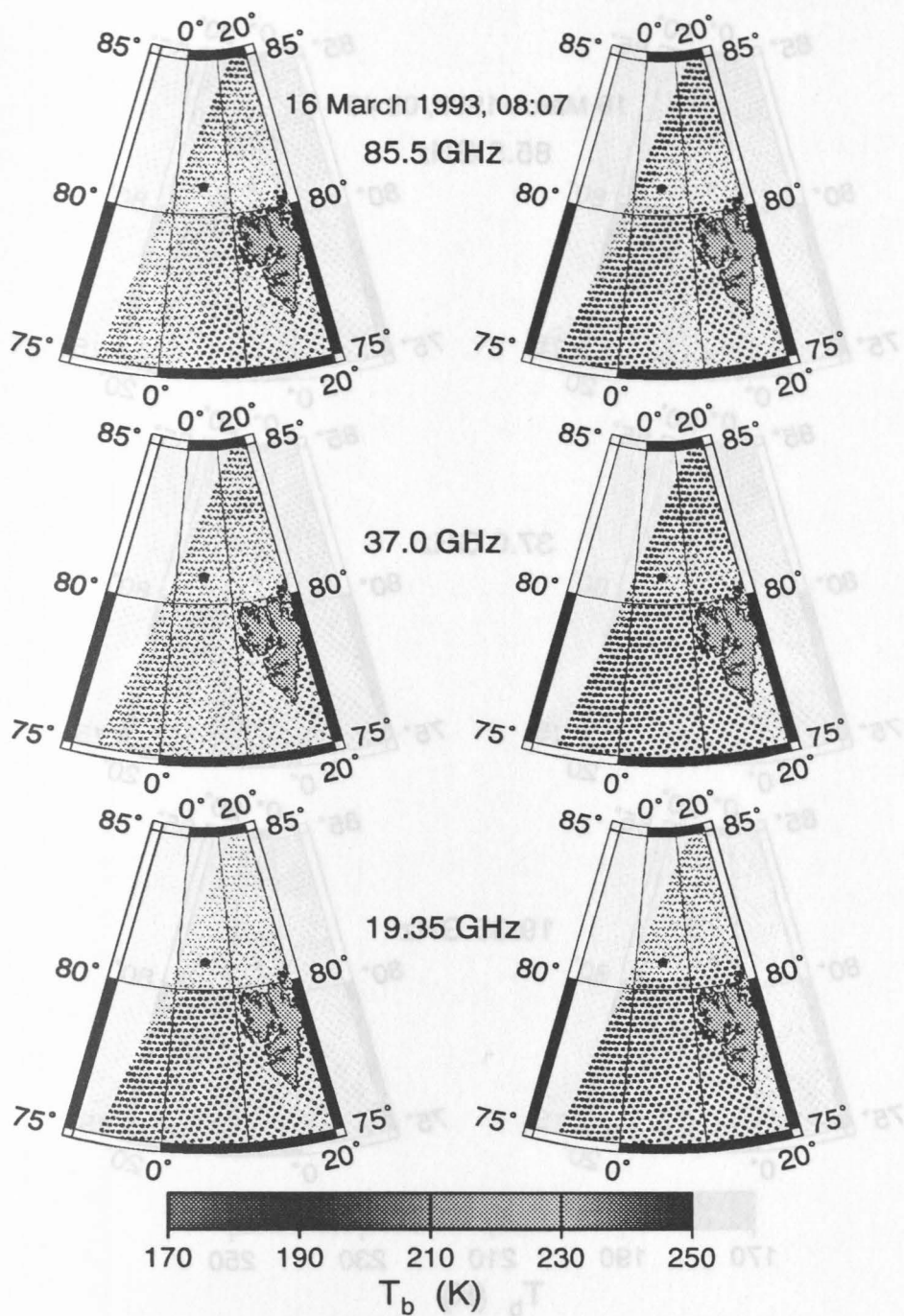


Figure 54 SSM/I brightness temperature distributions around the ice-floe station on 16 March 93, 08:07 UT; the station is indicated by the black bullet.

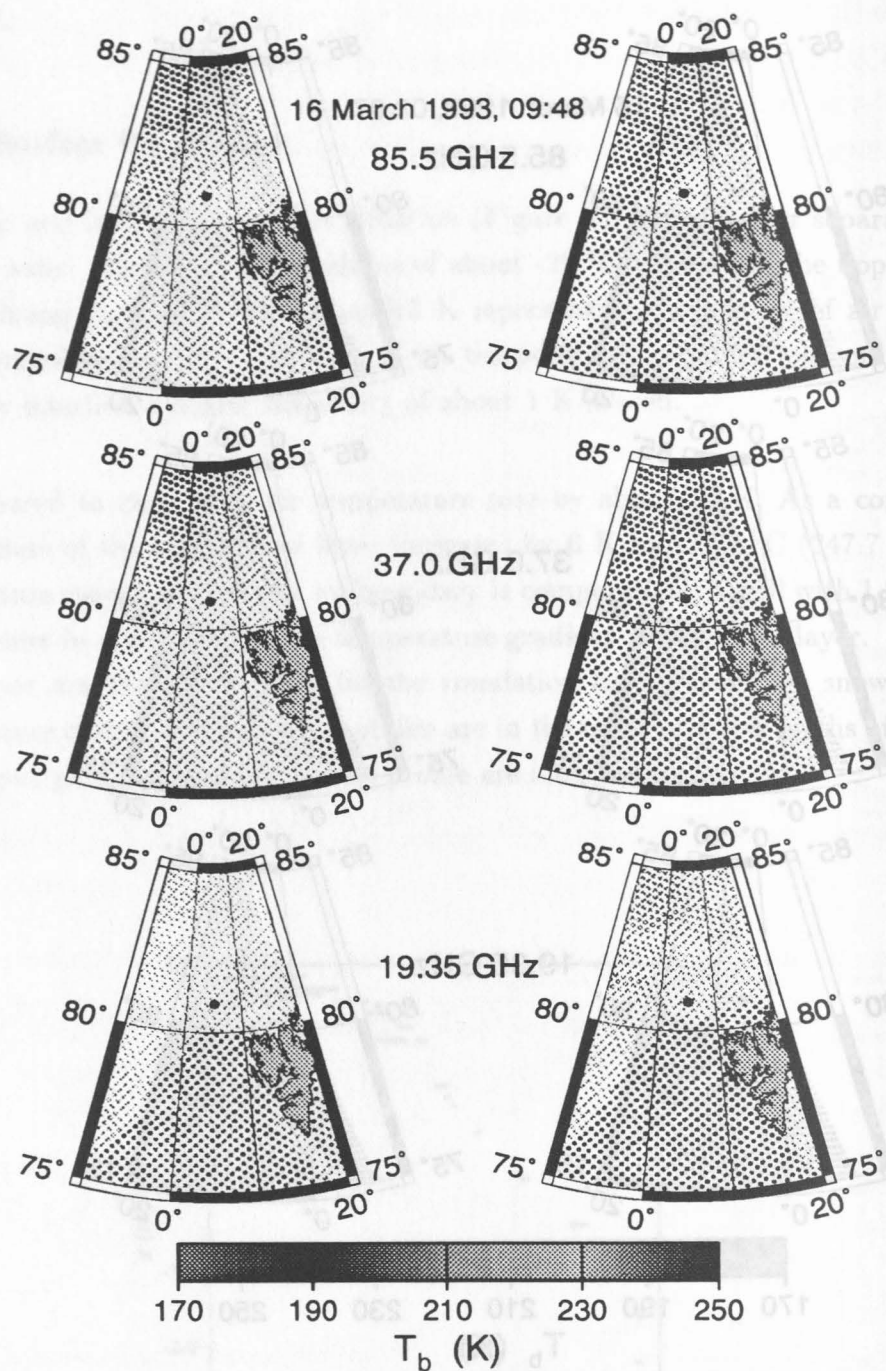


Figure 55 SSM/I brightness temperature distributions around the ice-floe station on 16 March 93, 09:48 UT; the station is indicated by the black bullet.

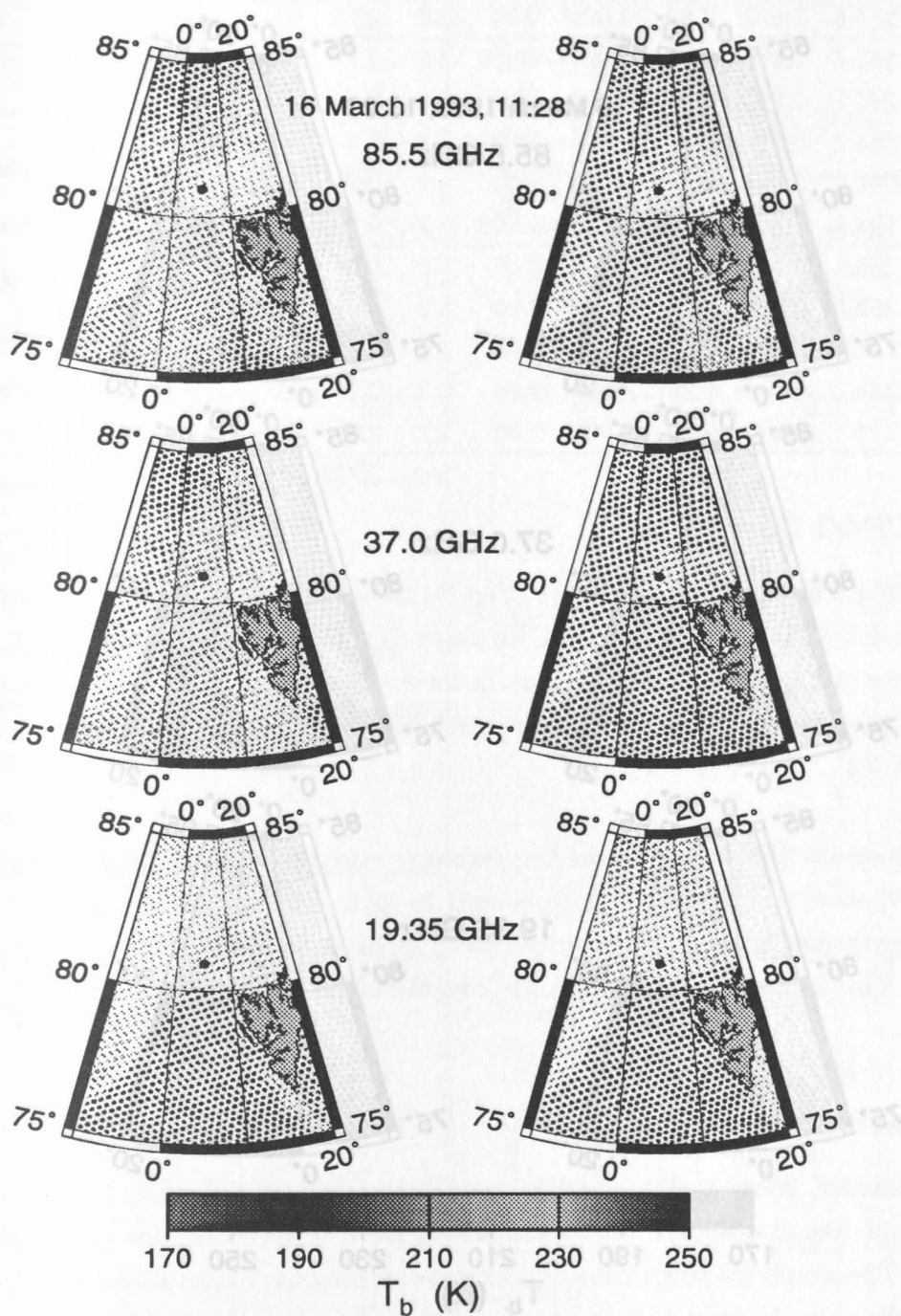


Figure 56 SSM/I brightness temperature distributions around the ice-floe station on 16 March 93, 11:28 UT; the station is indicated by the black bullet.

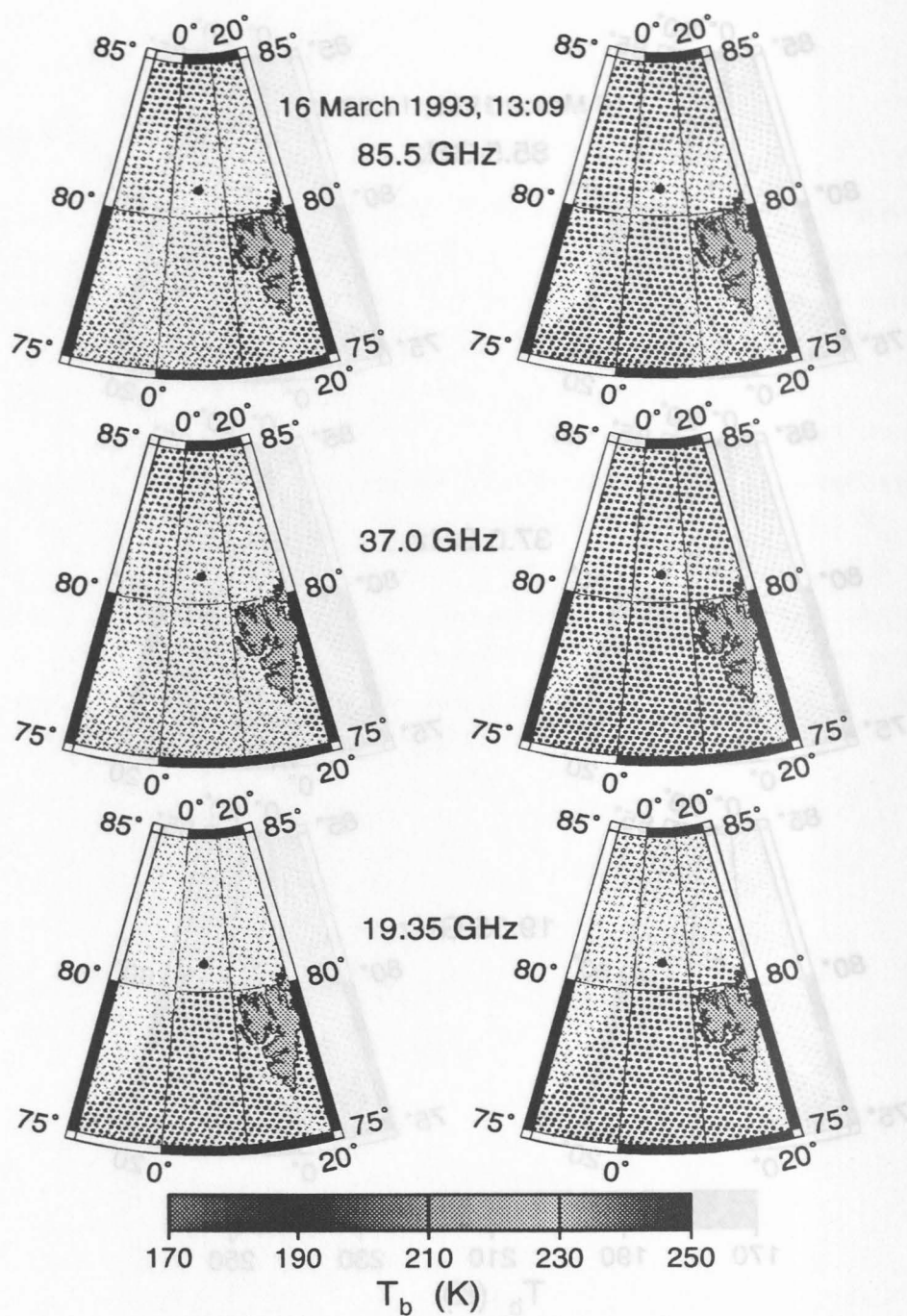


Figure 57 SSM/I brightness temperature distributions around the ice-floe station on 16 March 93, 13:09 UT; the station is indicated by the black bullet.



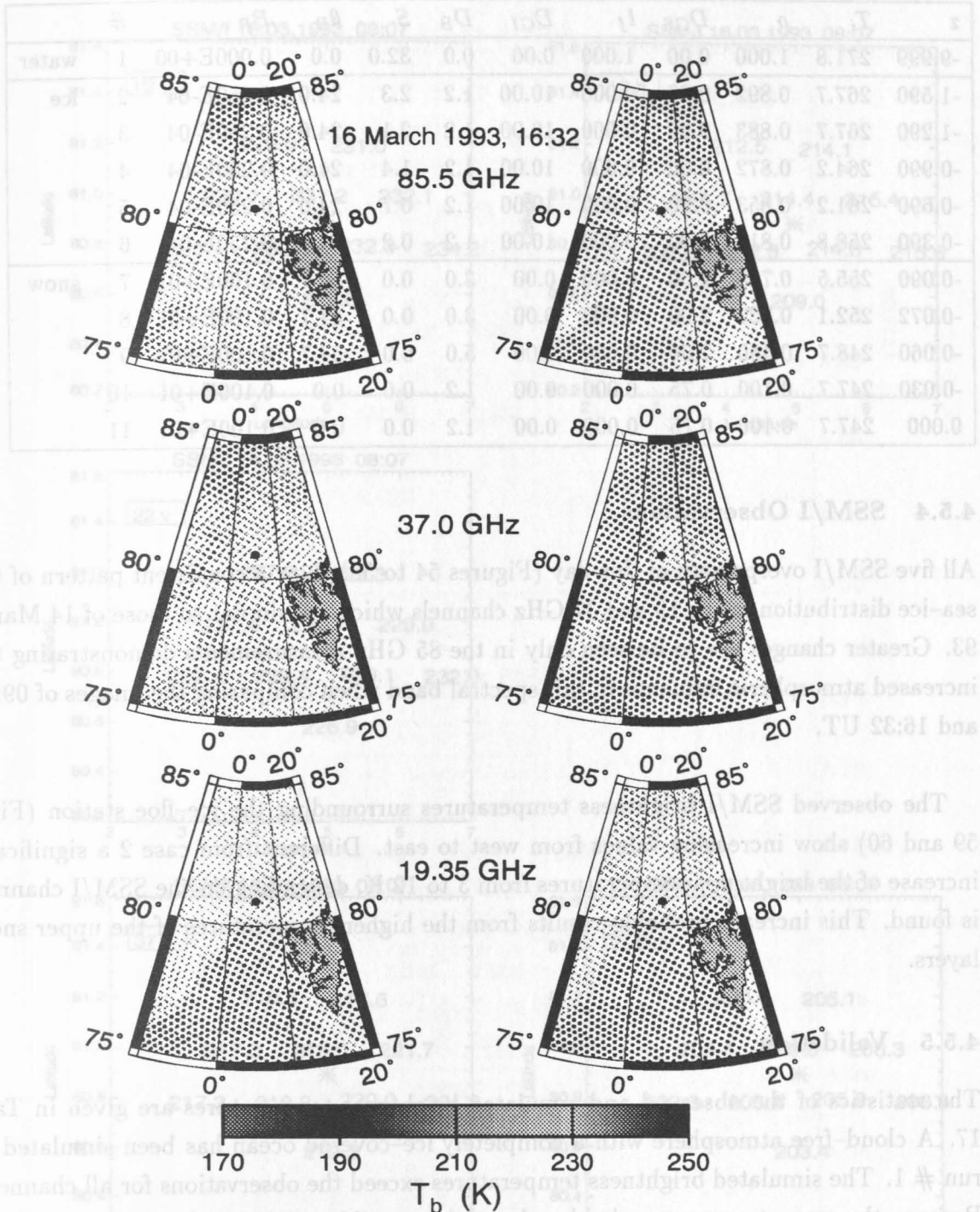


Figure 58 SSM/I brightness temperature distributions around the ice-floe station on 16 March 93, 16:48 UT; the station is indicated by the black bullet.

**Table 16** Input parameter for sea ice module for case 3. For explanation of the parameters see Tab. 6

$z$	$T_i$	$\rho$	$D_{GS}$	$l_f$	$D_{GI}$	$D_B$	$S$	$\theta_B$	$B_R$	#	
-9.999	271.8	1.000	0.00	1.000	0.00	0.0	32.0	0.0	0.000E+00	1	water
-1.590	267.7	0.892	0.00	0.000	10.00	1.2	2.3	24.0	0.250E-04	2	ice
-1.290	267.7	0.883	0.00	0.000	10.00	1.2	2.1	24.0	0.250E-04	3	
-0.990	264.2	0.872	0.00	0.000	10.00	1.2	1.4	24.0	0.250E-04	4	
-0.690	261.2	0.853	0.00	0.000	10.00	1.2	0.7	24.0	0.250E-04	5	
-0.390	258.8	0.814	0.00	0.000	10.00	1.2	0.2	24.0	0.250E-04	6	
-0.090	255.5	0.728	2.00	0.000	0.00	3.0	0.0	54.7	0.100E+01	7	snow
-0.072	252.1	0.728	2.00	0.000	0.00	3.0	0.0	54.7	0.100E+01	8	
-0.060	248.7	0.460	2.00	0.000	0.00	5.0	0.0	54.7	0.100E+01	9	
-0.030	247.7	0.100	0.75	0.000	0.00	1.2	0.0	0.0	0.100E+01	10	
0.000	247.7	0.100	0.75	0.000	0.00	1.2	0.0	0.0	0.100E+01	11	

#### 4.5.4 SSM/I Observations

All five SSM/I overpasses of this day (Figures 54 to 58) show a consistent pattern of the sea-ice distribution in the 19 and 37 GHz channels which are similar to those of 14 March 93. Greater changes are to be seen only in the 85 GHz measurements demonstrating the increased atmospheric influence in this spectral band when comparing the images of 09:48 and 16:32 UT.

The observed SSM/I brightness temperatures surrounding the ice-floe station (Figs. 59 and 60) show increasing values from west to east. Different from case 2 a significant increase of the brightness temperatures from 3 to 12 K, depending on the SSM/I channel, is found. This increase probably results from the higher temperatures of the upper snow layers.

#### 4.5.5 Validation

The statistics of the observed and simulated brightness temperatures are given in Tab. 17. A cloud-free atmosphere with a completely ice-covered ocean has been simulated in run # 1. The simulated brightness temperatures exceed the observations for all channels. Because the scene temperature is already at the possible minimum (temperature of the upper snow layer), a reduction of the simulated brightness temperatures can be achieved only by introducing clouds, open water areas, or changing the sea ice/snow profile.

A snow cloud with  $l = 0.03 \text{ kg m}^{-2}$  (simulation 2) shows a significant effect at only 85 GHz ( $\Delta T_{B,cl}$ ). Thus further changes of the environment are necessary to achieve an agreement between the observed and simulated brightness temperatures. The estimated



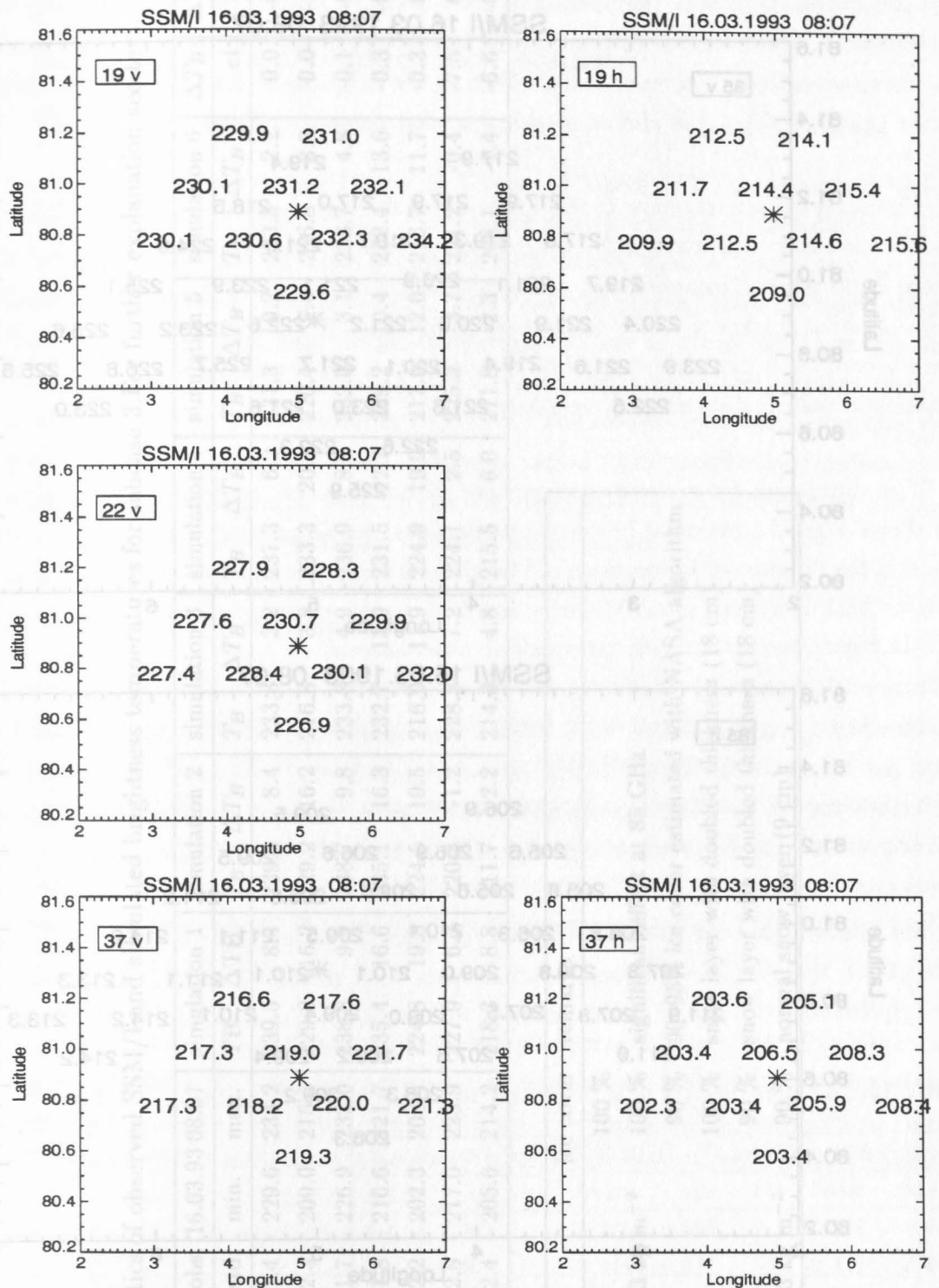


Figure 59 Observed SSM/I brightness temperatures (5 lower frequency channels) of the nearest pixels to ice-floe station (\*) for case 3.



Table 17 Statistics of observed SSM/I and simulated brightness temperatures for subcase 3. For further explanation see text.

SSM/I F11 $T_B$ obs. 16.03.93 08:07					simulation 1		simulation 2		simulation 3		simulation 4		simulation 5		simulation 6		$\Delta T_B$	$\Delta T_B$	$\Delta T_B$
chan.	mean	std.	min.	max.	TB	$\Delta T_B$	$T_B$	$\Delta T_B$	$T_B$	$\Delta T_B$	$T_B$	$\Delta T_B$	$T_B$	$\Delta T_B$	$T_B$	$\Delta T_B$	cl	ow	snow
19 v	231.1	1.4	229.6	234.2	239.5	8.4	239.5	8.4	233.3	2.2	237.3	6.2	231.3	0.2	233.3	2.2	0.0	-0.6	-2.2
19 h	213.0	2.3	209.0	215.6	229.2	16.2	229.2	16.2	216.8	3.8	233.3	20.3	220.4	7.4	216.8	3.8	0.0	-1.2	4.1
22 v	228.9	1.7	226.9	232.0	238.8	9.9	238.7	9.8	233.8	4.9	236.9	8.0	232.0	3.1	233.7	4.8	-0.1	-0.5	-1.9
37 v	218.8	1.8	216.6	221.7	235.4	16.6	235.1	16.3	232.7	13.9	231.5	12.7	229.2	10.4	232.4	13.6	-0.3	-0.3	-3.9
37 h	205.0	2.2	202.3	208.4	224.8	19.8	224.5	19.5	216.9	11.9	224.9	19.9	217.0	12.0	216.7	11.7	-0.3	-0.8	0.1
85 v	221.6	2.5	217.0	225.9	227.9	6.3	220.4	-1.2	228.8	7.2	224.1	2.5	225.3	3.7	221.2	-0.4	-7.5	0.1	-3.8
85 h	209.5	2.4	205.6	214.2	218.3	8.8	211.7	2.2	214.3	4.8	215.5	6.0	211.8	2.3	208.1	-1.4	-6.6	-0.4	-2.8

Sim.	cloud	ice cover	remarks
1	none	100 %	
2	snow 0.03 kg m <sup>-2</sup>	100 %	significant effect at 85 GHz
3	none	90 %	90–95% ice cover estimated with NASA algorithm
4	none	100 %	snow layer with doubled thickness (18 cm)
5	none	90 %	snow layer with doubled thickness (18 cm)
6	snow 0.03 kg m <sup>-2</sup>	90 %	normal snow layer (9 cm)

sea ice cover (using the NASA sea ice algorithm) is in the range from 90 to 95% in close agreement with the aircraft observations. The simulated brightness temperatures for an ice concentration of 90% (simulation 3) show reduced values, except for 85 GHz vertical polarization. However, the simulated brightness temperatures for 19 and 22 GHz are close to the observations. The open water effect on the brightness temperatures for 1% sea ice cover change ( $\Delta T_{B,ow}$ ) is almost identical to that computed for case 2.

Changing the sea ice/snow profile by doubling the snow layer to 18 cm (simulation 4) affect all channels significantly ( $\Delta T_{B,snow}$ ), except 37 GHz horizontal polarization. However, there is no general improvement of the comparison. Assuming an sea ice cover of 90% with doubled thickness of the snow layer (simulation 5) reduces the differences between the observed and modelled brightness temperatures, but the deviations for 37 and 19 GHz horizontal polarization are still very large.

The simulation for a cloudy atmosphere with a reduced ice cover of 90% (simulation 6) shows a good agreement between observations and simulation, except for 37 GHz. In general the differences to the observed brightness temperatures are smaller as for the simulation with increased snow thickness and 90% sea ice coverage. Furthermore, simulation 6 is in better agreement with the synoptic observations.

Comparing the simulation for a cloudy atmosphere and 90% ice cover (simulation 6) with the restored SSM/I data instead of the original SSM/I data exhibits an improvement especially for the 19 GHz channels (Tab. 18). Hence, it is deduced that the image restoration process reduces effects of the large footprint size for the 19 GHz channels.

For this test case the model is able to reproduce the observed brightness temperatures, except for the 37 GHz channels. Simulations with modified sea ice parameters show no improvement for the 37 GHz channels without a deterioration for the other channels.

Table 18 Restored SSM/I brightness temperatures for overpass 08.07 UT (case 3).

SSM/I F11 m37 rest. $T_B$ 16.03.93 08:07					simulation 6	
chan.	mean	std.	min.	max.	$T_B$	$\Delta T_B$
19 v	232.3	1.1	230.0	233.9	233.3	1.0
19 h	215.2	1.7	213.2	217.5	216.8	1.6
22 v	228.7	0.8	227.8	230.1	233.7	5.0
37 v	219.8	0.8	219.0	221.1	232.4	12.6
37 h	205.3	1.3	203.1	207.3	216.7	11.4
85 v	223.0	0.9	221.9	224.5	221.2	-1.8
85 h	210.4	0.9	209.1	211.7	208.1	-2.3

However, to achieve the agreement it is important to simulate the environmental conditions as they have been observed.

4.6 Case 4: Ice, partly cloudy sky, winter

4.6.1 Synoptic Situation

Case 4 is a short period between 11 and 17 UT on 18 March 1993, characterized by low cloud coverage (less than three octas). The ice-floe station, drifted to the location 5.0°E, 80.6°N, still lies in a cold air mass separated by a frontal system from warm air over the Barents and southern Greenland Seas. The wind was blowing from the north with a speed of about 12 m/s, that kept the air temperature as low as about -30 °C on this day. The water temperature slightly rised to -1.4°C when compared to the previous case. A light snow drift caused a low visibility (<9 km). The clouds observed during this day were mainly at middle and high levels, the types varied from altostratus translucidus to cirrocumulus and stratocumulus stratiformis. No precipitation was observed on this day. Table 19 summarizes the synoptic data used for the simulation.

4.6.2 Atmospheric Parameters

Again, three radiosonde ascents are available for this situation. All temperature profiles show a pronounced temperature inversion below 900 hPa. Smaller inversions are identified near 820 and 710 hPa at 10:17 UT and near 780 hPa at 16:26 which are not seen in the profile at 04:29 UT. Despite these meteorologically important differences the first two profiles look quite similar and show drastic differences, up to 8K, to the last profile. In the afternoon the top of the near-surface inversion is lifted to a higher level and lower temperature. Between about 750 and 550 hPa the temperatures are higher by up to 2 K than in the morning profiles.

The humidity structure undergoes strong changes during this day, too. The large scale subsidence connected with the high-pressure system causes a drying of the upper troposphere where relative humidities decrease from maximum values near 85% to values between 10 and 40%. Between 850 and 500 hPa the humidity also strongly decreases

Table 19 Synoptic observations for case 4.

date : 18.3.1993	position : 4.96 <sup>0</sup> E / 80.65 <sup>0</sup> N	
SSM/I overpass : 09:22 UT	radiosonde launch : 04:29 UT	synop : 09 UT
pressure : 1000.2 hPa	$T_a$ : -29.2 °C	humidity : 78 %
wind speed : 14.9 m/s	$T_0$ : -1.4 °C	cloud : 6605-
wind dir. : 9 °	PWC : 3.3 kg m <sup>-2</sup>	$\Delta T_{ice-snow}$ : -11.9 K